A novel variant in MFN2 linked to a lethal disorder of neonatal onset

Authors: Mashiat Zaman[1], Cole Chute[1], Julien L Marcadier[2], S Grewal[1], R Luke Wiseman[3], Amanda V Tyndall[4], Brenda McInnes[2], A Micheil Innes[5], Francois P Bernier[5], Timothy E. Shutt[6*]

[1]Department of Biochemistry & Molecular Biology, Cumming School of Medicine, Hotchkiss Brain Institute, Alberta Children's Hospital Research Institute, University of Calgary

[2]Department of Medical Genetics, Cumming School of Medicine, University of Calgary

[3]Department of Molecular and Cellular Biology, The Scripps Research Institute, La Jolla, CA

[4]Department of Medical Genetics, Cumming School of Medicine, Alberta Children's Hospital Research Institute, Hotchkiss Brain Institute, University of Calgary

[5]Departments of Medical Genetics and Pediatrics, Cumming School of Medicine, Alberta Children's Hospital Research Institute, University of Calgary

[6]Departments of Medical Genetics and Biochemistry & Molecular Biology, Cumming School of Medicine, Hotchkiss Brain Institute, Snyder Institute for Chronic Diseases, Alberta Children's Hospital Research Institute, University of Calgary

*Corresponding author (timothy.shutt@ucalgary.ca)

Abstract:

Pathogenic variants in the mitochondrial fusion protein Mitofusin2 typically cause axonal Charcot-Marie-Tooth disease type 2A (CMT2A), a progressively degenerative peripheral neuropathy. Here, we present two siblings with a lethal disorder of neonatal onset who carried a novel homozygous MFN2 variant R334K, which was predicted to be likely pathogenic. Given the severe clinical presentation, which is atypical of MFN2 variants, further functional investigations were warranted to confirm the pathogenicity of the R334K variant. Characterization of patient fibroblasts showed severe disruptions all MFN2-related functions that were assayed, including mitochondrial fragmentation, altered mito-ER contacts, decreased mtDNA copy number and size, increased abundance of cellular lipid droplets, and reduced mitochondrial respiration. We also observed reduced Complex I activity, which is noted in cells lacking MFN2, but is not typical of pathogenic MFN2 variants that cause CMT2A. Notably, re-expression of MFN2 R334K in MFN2 knockout cells was unable to rescue mitochondrial fragmentation and the Complex I deficiencies, confirming that the R334K variant is causative of these cellular phenotypes. Furthermore, disease modelling in *Drosophila melanogaster* demonstrated functional deficiencies of the R334K variant *in vivo*. Together, these findings confirm that the MFN2 R334K is a novel pathogenic variant causing severe fatal neonatal disease patient pathology. Finally, we show that pharmacological activation of the integrated stress response rescues defects caused by MFN2 R334K, offering a potential therapeutic avenue for MFN2 pathology.

38 **Introduction:**

39 Pathogenic variants in *MFN2* cause the hereditary motor sensory neuropathy Charcot-
40 Marie-Tooth disease 2a (CMT2a), which is characterized by progressively worsening pain,
41 numbness and weakness in the distal regions of the body. CMT2a is generally seen as an early-
42 onset disease, with symptoms typically appearing around the age of 10. While CMT2a is most
43 often autosomal dominant (CMT2A2A), there are cases of homozygous or compound
44 heterozygous recessive inheritance (CMT2A2B) [25, 46]. *MFN2* encodes the integral outer
45 mitochondrial membrane (OMM) protein Mitofusin2 (MFN2), initially characterized for a role in
46 mitochondrial fusion [12]. The protein consists of distinct domains, with an N-terminal GTPase
47 domain, followed by two coiled-coiled heptad repeat (HR) domains separated by a
48 transmembrane domain.

49 The clinical presentation of CMT2a can vary widely, where some MFN2 variants are
50 associated with additional patient pathology [29, 53, 54*]*. While there is evidence of specific
51 MFN2 variants leading to severe and early pathology, neonatal lethality is exceedingly rare [7,
52 13, 15, 21]. Though the reasons for this heterogeneity are unknown, it is notable that MFN2 has
53 several other functions, including mediating mito-ER contacts (MERCs) [10]**,** facilitating mito-
54 lipid droplet contacts [9], participating in mitochondrial transport [40] and being a key regulator
55 of mitophagy [38]**.** These MFN2 functions also influence downstream processes such as mtDNA
56 regulation [55], cellular Ca^{2+} signalling [1] and mitochondrial bioenergetics [64]. The impact of
57 different MFN2 variants on the various functions of MFN2 is largely unknown [64]. Surprisingly,
58 for the few variants that have been studied, fusion is not always impacted [2, 16, 30, 33, 63],
59 suggesting that other MFN2 functions are also important in the context of pathology.

60 There is no cure for CMT2A or other pathologies associated with MFN2 dysfunction.
61 Though several promising preclinical approaches are in development [49, 50, 62], they are
62 focused primarily on promoting mitochondrial fusion, rather than other MFN2 functions.
63 Building on the fact that activation of the Integrated Stress Response (ISR) has recently
64 garnered attention for ameliorating mitochondrial dysfunction [1, 31, 40, 54], we recently
65 showed that ISR activation can restore mitochondrial morphology in patient fibroblasts

66 harbouring the pathogenic D414V MFN2 variant [5], as well as MERCs, mitochondrial motility,
67 and mitochondrial respiration in MFN2 KO cells [8] . ISR activation is mediated by
68 phosphorylation of eIF2α via four kinases that sense different types of cellular stress (*i.e.*, HRI,
69 GCN2, PERK and PRK), ultimately turning on the ATF4 transcription factor that engages multiple
70 cellular stress responses. Thus, ISR activation is a promising therapeutic approach to target
71 mitochondrial dysfunction beyond just impaired mitochondrial fusion.

72 In this work, we describe two siblings who presented with areflexia, hypotonia and
73 restricted movement upon birth, and who harbored a novel homozygous variant of unknown
74 significance in MFN2, c.1001G>A, p.(Arg334Lys), which was deemed worthy of further
75 investigation. We report detailed patient pathology and provide a comprehensive fibroblast
76 characterization of multiple mitochondrial functions associated with MFN2. Using cell and
77 animal modeling, we also provide evidence that the R334K MFN2 variant is dysfunctional and is
78 sufficient to explain the cellular phenotypes and severe patient pathology. Finally, we show that
79 ISR activation rescues mitochondrial fragmentation and reduced respiration in R334K patient
80 fibroblasts, offering a promising therapeutic avenue for MFN2-mediated pathology.

81 **Methods**

82 **Genomic analysis**

83 The proband was enrolled into a research study titled Rapid Access for Pediatric
84 Diagnoses Kidomics (RAPiD) at the Alberta Children's Hospital. Formal written consent was
85 provided by the family (mother, father, and proband) for both the RAPiD research exome (study
86 approved by the University of Calgary Conjoint Health Research Ethics Board) sequencing and
87 the clinical whole exome sequencing. DNA was extracted from whole blood samples, and trio
88 exome library preparation was conducted using the xGen Exome Research Panel v1.0 capture
89 kit (Integrated DNA Technologies, Inc., Coralville, IA, USA). Paired-end sequencing was
90 performed on a NextSeq 550 (Illumina, San Diego, CA, USA) in which data was automatically
91 uploaded into BaseSpace Sequencing Hub where alignment, variant calling, and variant
92 interpretation was completed.

93 **Sequence alignment**

94 Amino acid sequence alignments for MFN2 and FOXRED1 were performed on T-COFFEE
95 multiple sequence alignment tool [17]. Protein sequences were collected from the UniProt
96 database [58]. The UniProt Sequence ID's were as follows: Human MFN2: O95140-1; Human
97 MFN1: Q8IWA4; Mouse MFN2: Q80U63; Fish MFN2: A8WIN6; Fly MFN2: Q7YU24; Worm
98 MFN2: Q23424; FXRD1: Q96CU9; FXRD1 [2]: Q96CU9-2 ; FXRD1 [3]: Q96CU9-3; Mouse FXRD1:
99 Q3TQB2; Fish FXRD1: A0A0R4IHD6; Fly FXRD1: Q9VJ10; Worm FXRD1: A0A0V1BI76 .

100 **Cell culture**

101 Skin fibroblasts were cultured in Minimum Essential Media (Gibco™, 11095098),
102 supplemented with 10% Fetal Bovine Serum (FBS) and 10mM Sodium Pyruvate. The cells were
103 maintained at 37°C and 5% CO_2. U2OS cells were maintained in DMEM high-glucose media
104 (Gibco™; 11965118), also at 37°C and 5% CO_2. The following ISR inhibitors/activators were used
105 for the morphology and OCR studies: ISRIB (ISR inhibitor) (Cat# SML0843, Sigma), halofuginone
106 (Cat#50-576-3001, Sigma), #3610 or Parogrelil (139145-27-0, Axon Medchem). For drug

107 treatments the compounds were added at the following doses: ISRIB (200nM), compound
108 #3610 (10uM), Parogrelil (10uM) and Halofuginone (100nM),

109 **Respiration studies**

110 Cellular oxygen consumption rates were measured using the Seahorse XFe24
111 Extracellular Flux Analyzer (Agilent Technologies) as previously described [52]. In summary, cells
112 were seeded in the manufacturer provided microplate at 70,000 cells/well and incubated for 24
113 hours at 37°C and 5% CO_2. Subsequently, the growth media was replaced, and cells equilibrated
114 in assay media supplemented with d-Glucose (25 mM), sodium pyruvate (2 mM) and l-
115 Glutamine (4 mM). Oxygen consumption rates were calculated following administration of the
116 following compounds: Oligomycin (1 µg/mL) (Enzo Life Sciences, BML-CM111), Carbonyl
117 Cyanide 4-(trifluoromethoxy) Phenylhydrazone (FCCP, 1 µM) (Enzo life Sciences, BML-CM120)
118 and Antimycin A (1 µM) (Sigma Aldrich, A8674). The data from the Seahorse analyzer was
119 normalized to protein content data for each well measured by BCA assay (Thermo Fisher
120 Scientific, 23225). The Lucid Resipher assay was used for the ISR studies, as previously
121 described [8]. Briefly, 15,000 cells were seeded on a round bottom 96-well cell culture plate
122 (MaxBioChem, MBC.TC.F. 96)and allowed to settle for 18 hours. The ISR inhibitors/activators
123 were added at the following doses: ISRIB (200nM), compound #3610 (10uM), Parogrelil (10uM)
124 and Halofuginone (100nM):, and OCR was measured at 6 hours after treatment. Samples were
125 normalized for total protein content, lysed from the 96-well plate using RIPA buffer (Thermo
126 Scientific™, 89900) using a BCA assay, standardized with BSA (Fisher Scientific, PI23209).

127 **Immunofluorescence and Microscopy**

128 20,000 control/patient fibroblasts or U2OS cell lines were seeded on 12mm
129 (Fisherbrand, 12-545-81) coverslips inserted into wells of a 24-well plate (Sarstedt, 83.3922)
130 and incubated for 24 hours at 37°C and 5% CO_2. Cells were fixed with 4% paraformaldehyde
131 (ElectronMicroscopySciences, 15710) at 37°C for 20 minutes, permeabilized using 0.1% Triton®
132 X-100 (MP Biomedicals, 9002-93-1) and blocked with 10% FBS. The mitochondrial network was
133 stained with anti-TOMM20 (Sigma-Aldrich, HPA011562/Santa Cruz Biotechnology, F-10 sc-
134 17764) primary antibodies and visualized using goat anti-rabbit secondary conjugated with

135 Alexa Fluor 488 (ThermoFisher, A-11034) or goat anti-mouse conjugated Alexa Fluor
136 (ThermoFisher, A-31571). Mitochondrial nucleoids were visualized using anti-dsDNA antibody
137 (Developmental Studies Hybridoma Bank, AB_10805293) and goat anti-mouse secondary
138 conjugated with Alexa fluor 568 (ThermoFisher, A-11004), following permeabilization with 0.2%
139 Triton® X-100). Lipid droplets were tagged using anti-PLIN1 antibody (Cell Signalling
140 Technology, 9349S). Confocal imaging was performed using Olympus spinning disc confocal
141 system (Olympus SD OSR) (UAPON 100XOTIRF/1.49 oil objective). STED imaging was performed
142 using Leica TauSTED microscope. For the ISR studies, control and patient fibroblasts were
143 seeded at 70,000 cells onto 35mm live cell imaging dishes (D35-20-1.5-N, Cellvis) and allowed
144 to settle for 24 hours. Mitochondrial networks were stained with 100nM MitoTracker Green FM
145 (M7514, Life Technologies) for 30 minutes and subsequently washed with cell culture media
146 three times. . Z-stacks were captured using confocal imaging was performed using Olympus
147 spinning disc confocal system (Olympus SD OSR) (UPlanApo. 60X 1.50NA), including a cellVivo
148 live cell incubator system used to maintain cells at 37°C and 5% CO_2 , Mitochondrial
149 morphology was qualitatively scored based on appearance categorized into
150 fused/intermediate/fragmented for 150 cells, spread across 3 biological replicates. Quantitative
151 mitochondrial network analyses were performed using MiNA on FIJI [59], also scored for 150
152 cells, spread across 3 biological replicates .

153 **Proximity Ligation Assay:**

154 The proximity ligation assay was performed as mentioned in [54]. All immunostaining
155 steps, including fixation, blocking and permeabilizing were the same as mentioned for
156 mitochondrial network studies. The Duolink® In Situ Proximity Ligation Assay (Millipore Sigma)
157 was used for this. The aforementioned anti-TOMM20 antibody was used to label the
158 mitochondria, while the ER was labelled using anti-Calnexin (mouse monoclonal, EMD
159 Millipore: MAB3126 (RRID:AB_2069152). Images were analyzed using confocal microscopy (as
160 described above) and PLA puncta were analyzed using the 'analyze particles' tool on FIJI.

161

162

163 **Western Blot Analysis**

164 Cells grown to the same confluency were collected and RIPA buffer (Thermo Scientific™,
165 89900) complimented with protease inhibitors (VWR, 97063-010) was used to lyse and collect
166 the protein extracts. For fly protein, 20 flies were homogenized and sonicated in RIPA buffer
167 (Thermo Scientific™, 89900). Following quantification of protein concentrations using a BCA
168 assay, standardized to BSA (Fisher Scientific, PI23209), 50 µg of total protein was loaded on an
169 SDS-PAGE gel. Subsequently, PVDF membranes (Bio-Rad, 1620177) were used for overnight
170 transfer of the blots. The blots were probed with the following antibodies: anti-MFN2 (Abnova,
171 H00009927-M03; 1:1000), anti-MFN1 (Cell Signaling Technology, D6E2S; 1:1000), anti-OPA1 (BD
172 Transduction Laboratories, 612607; 1:1000), anti-Actin (Sigma, A5316; 1:1000) anti-Actin for fly
173 membrane (DSHB, JLA20; 1:1000) and cocktail anti-OXPHOS Complex antibody (AbCam,
174 ab110411; 1:500). Complimentary horseradish peroxidase conjugated antibodies were used:
175 goat anti rabbit IgG, HRP linked Antibody (Cell Signaling Technology, 7074S) or goat anti-mouse
176 IgG-HRP (Santa Cruz Biotechnology, sc-2055). Blots were treated with the SuperSignal™ West
177 Femto Maximum Sensitivity Substrate (Thermo Scientific™, 34095), and luminescence
178 visualized with an Amersham Imager AI600.

179 **mtDNA Copy Number and mtDNA Deletions Analysis**

180 Total DNA was extracted and purified from control and patient fibroblasts seeded at
181 30,000 cells using the PureLink Genomic DNA Mini Kit (Thermo Fisher Scientific, K182001) using
182 the given protocol. Relative mtDNA copy number was analysed using QuantStudio 6 Flex Real-
183 Time PCR system (Thermo Fisher Scientific). The mtDNA and nuclear encoded housekeeping
184 gene 18S were amplified using the primers and reaction conditions described in [18]. Long
185 range PCR reactions were performed to examine mtDNA deletions. The following primers were
186 used for amplification of the mtDNA: 1482–1516 F:
187 ACCGCCCGTCACCCTCCTCAAGTATACTTCAAAGG; 1180–1146 R:
188 ACCGCCAGGTCCTTTGAGTTTTAAGCTGTGGCTCG. The Takara LA Taq Polymerase (Takara Bio,
189 RR002M) was used with 250ng total cellular DNA. PCR cycling conditions were 94°C for 1 min;
190 98°C for 10 s and 68°C for 11 min (step 2 and 3- 35 cycles); and a final extension cycle at 72°C

191 for 10 min, using an Eppendorf® 5331 MasterCycler Gradient Thermal Cycler. PCR products
192 were visualized by electrophoresis on a 0·6% agarose gel, run for approximately 18 h at 20 V.

193 **Complex-I Activity Assay**

194 The mitochondrial complex-I activity assay was performed using the Complex I Enzyme
195 Activity Dipstick Assay Kit (AbCam, ab109720) according to manufacturer instructions. Briefly,
196 50,000 cells were seeded into a six-well plate (Sarstedt, 83.3920) and collected the following
197 day. 10x Extraction buffer from the kit was added to the cell pellet and subsequently spun at
198 18,000 x g. Supernatants were collected and following homogenization, control and patient
199 samples were plated in the plate provided. Subsequently, the dipstick from the plate was added
200 and incubated for 45 minutes. Following washing procedures, the dipsticks were imaged with
201 Amersham Imager AI600.

202 **Re-expression of MFN2 R334K in U2OS cells:**

203 U2OS MFN2 knockout cells were a generous gift from Dr. Edward Fon (McGill University,
204 Canada) [38]. The MFN2 R334K variant was inserted into MFN2 KO cells as previously described
205 [63]. Briefly, a retroviral plasmid vector (Vector Builder, VB230626-1399nzw) with the MFN2
206 R334K open reading frame or WT MFN2, followed by an mNeonGreen (after IRES) was virally
207 inserted into MFN2 KO cells, and cells were sorted for mNeonGreen expression through
208 fluorescence activated cell sorting. Endogenous expression levels were quantified by western
209 blot analysis, as described in the western blot section of methods.

210 ***Drosophila* stocks, transgenic lines and experiments**

211 All *Drosophila* were maintained at 25°C and kept in standard food. Flies were allowed to
212 lay eggs on standard grape plates with yeast plated for two days before collection. *Drosophila*
213 stocks for ey3.5-Gal4 (BDSC#8221) was provided by Dr. William Brook (University of Calgary,
214 Canada), elav-Gal4, tub-Gal4 (BDSC#5138), act5c-Gal4 (BDSC#4414), daGal4, UAS-*mCherry*RNAi
215 and UAS-*marf* RNAi (31157) [44] was provided by Dr. Savraj Grewal (University of Calgary,
216 Canada) and tincΔ4Gal4 was provided by Dr. Rolf Bodmer (Sanford Burnham Prebys Medical
217 Discovery Institute, USA). A second UAS-*marf*RNAi (67158) was purchased from Bloomington

218 Stock Centre (Indiana University, USA). Flies re-expressing the human MFN2 WT and MFN2
219 R334K were generated through microinjection (GENOMEPROLAB, Canada). The pGW.UAS
220 hMFN2 plasmid used for microinjection was provided by Dr. Paul Marcogliese (University of
221 Manitoba, Canada), which was subsequently mutated by in-fusion cloning (Takara, 638945).
222 Flies were microinjected on chromosome II using the attp40 landing site, through the phiC31
223 integration approach. For the survival assay, flies were allowed to lay eggs on grape plates with
224 yeast paste for 48 hours and subsequently 50 eggs were collected and placed into standard
225 food. The number of eggs that became pupa were counted and normalized to total number of
226 eggs collected, for percentage survival. For negative geotaxis studies, 30 newly emerged adult
227 flies of the respective crosses were placed into a 1000cc cylinder. On a given day, the flies were
228 gently displaced to the bottom every 3 hours and the percentage of flies that made it past the
229 10 cm mark after 10 seconds was counted.

230 **Statistical Analyses**

231 All statistical analyses were performed using GraphPad Prism 9.

232 **Results:**

233 **Case description:**

234 Proband (P1)

235 The male proband was born by C-section for preterm labor, breech presentation and
236 fetal heart rate abnormalities at 35 weeks to a 21-25-year-old G3, P0 mother. The pregnancy
237 was remarkable only for a mild COVID infection in the first trimester with three antenatal
238 ultrasounds reported as completely normal. Decreased fetal movements were noted in the last
239 4 to 8 weeks of the pregnancy. His birthweight was 2.08 kg (10th percentile), length 46.6 cm
240 (50th percentile) and his head circumference was 32.1 cm (50th percentile). APGARs were
241 1,3,3,6 at 1, 5,10 and 15 minutes respectively. He remained flat with no respiratory effort and
242 was intubated at 6 minutes of life. He remained ventilator dependent and eventually died in
243 the pediatric intensive care unit at 2-6 weeks of age. On examination he was noted to have
244 hypotonia both peripherally and axially with decreased spontaneous movements. He had
245 bilateral flexion contractures at his elbows and knees with limited hip abduction and talipes
246 equinovalgus. He was noted to have a bulbous nasal tip but a complete dysmorphology exam
247 was not feasible.

248 Investigations included normal newborn metabolic screening, normal rapid aneuploidy
249 detection, SNP chromosomal microarray, Prader Willi, DM-1 and SMA. While chromosomal
250 microarray analysis did not reveal any copy number variation to explain the proband's
251 phenotype, the SNP component of the analysis revealed three contiguous regions (greater than
252 10Mb) of absence of heterozygosity (AOH) within chromosomes 1, 3, and 4. Metabolic
253 investigations revealed normal urine and plasma amino acids and a normal plasma acylcarnitine
254 profile. Urine organic acids were non diagnostic and plasma 3-methylglutaconic acid and 3-
255 methylglutaric acid were also normal. EEG was indicative of moderate diffuse/multifocal
256 cerebral dysfunction with multifocal epileptiform discharges. Brain MRI shortly after birth
257 showed multiple foci of diffusion restriction due to cytotoxic edema involving the deep and
258 periventricular white matter in frontoparietal lobes with corresponding intrinsic T1
259 hyperintensity. There were no overt signs on imaging or MRS to suggest a metabolic cause. A

260 follow-up brain MRI just prior to death reported interval resolution of the multiple foci of
261 restricted diffusion in the bilateral centrum semiovale ovale/corona radiata, with a few small
262 scattered residual centrum semiovale T1 hyperintense foci without restricted diffusion. As
263 compared to the previous MRI, there was interval development of atrophy of the superior
264 vermis, seen as increased interfoliate distance. Mild atrophy was also seen involving the lateral
265 cerebellar hemispheres. The brain stem structures, especially the midbrain and pons, had
266 reduced volume for patient's age, with prominence of the prepontine cisterns, resulting in
267 prominence of the posterior fossa CSF spaces without mass effect. The remainder of the
268 midline structures appeared normal with no Chiari I deformity and a normal pituitary gland. The
269 corpus callosum was well developed and the remaining brain parenchyma was normal with an
270 age-appropriate myelination pattern. No new areas of restricted diffusion or abnormal signal
271 involving the cerebrum or cerebellum were observed and there was no abnormal susceptibility-
272 related signal loss to suggest blood degradation products. The brain stem structures, especially
273 the midbrain and pons had reduced volume for the patient’s age. Additional imaging of the
274 patient’s spine showed marked smooth hypoplasia and reduced caliber of the thoracic spinal
275 cord. In addition, the brainstem and thoracic spinal cord reported to be small.

276 A muscle biopsy was performed shortly before death revealing no definite abnormalities
277 but coarse NADH, SDH, and COX histochemistries were observed in addition to mild
278 mitochondrial aggregation in the subarcolemmal spaces with some smaller mitochondria but
279 normal cristae. There were grouped atrophic fibres and occasional hypertrophic fibres.

280 Proband's sibling (P2)

281 The proband's male sibling presented with the same core phenotype of encephalopathy,
282 hypotonia, hyporeflexia, arthrogryposis. The sibling had an unremarkable prenatal history with
283 normal anatomy scan. A second scan at revealed breech presentation but otherwise normal
284 with normal fetal movements. A further scan was appropriate for gestational age and showed
285 breech presentation. He was born via C-section due to preterm labor with APGARS 1, 2, and 3
286 at 1, 5 and 10 minutes respectively, with no spontaneous respirations. He was intubated and
287 admitted to NICU. He required continuous mandatory ventilation. Life sustaining measures

288 were withdrawn between day 11-15 and the patient died the same day. An autopsy was
289 declined.

290 On examination at birth, the baby was noted to be hypotonic with contractures and
291 decreased range of motion of elbows, hips and knees with bilateral talipes equinovarus. His
292 birth weight was 2.365kg (<50th percentile), length 48 cm (<90th percentile) and head
293 circumference 31.4 cm (50th percentile). He had depressed/absent reflexes. Investigations
294 included a normal newborn metabolic screen, normal lactates, ammonia, and liver enzymes
295 with a mildly elevated CK. An EEG was consistent with encephalopathy. Brain MRI showed
296 cerebellar hypoplasia with query germiolytic cysts. An MRI of the spine was normal.

297 **Genetic workup**:

298 Upon initial research RAPID exome sequencing, trio analysis of P1 and parents, who
299 were distantly consanguineous, detected the homozygous c.1001G>A, p.(Arg334Lys) variant of
300 uncertain significance in the MFN2 gene. Pathogenic variants in MFN2 are associated with
301 autosomal dominant and autosomal recessive Charcot-Marie-Tooth disease, axonal, type 2A.
302 While patients with variants in MFN2 have a heterogeneous clinical presentation with an age of
303 onset ranging from 1-45 years, previously reported individuals with homozygous or compound
304 heterozygous variants presented before the age of 10 years [41, 57]. These affected individuals
305 presented with muscle weakness, distal sensory loss, and normal or mildly decreased nerve
306 conduction velocity, while the heterozygous parents were reported to be asymptomatic or had
307 signs of a mild peripheral neuropathy [41]. This variant has not been reported in gnomAD,
308 ClinVar, or the literature. This missense variant resides near the middle of exon 10 of 19 and
309 appears to abolish a potential cryptic donor splice site within this exon. The consequence of the
310 loss of this cryptic donor splice site is unknown. A subsequent clinical exome of P1 confirmed
311 the homozygous MFN2 c.1001G>A, p.(Arg334Lys) variant, and also found a novel homozygous
312 missense variant of unknown significance, c.1454T>A, p.(Ile485Asn), in FOXRED1, a gene
313 associated with complex I deficiency [4, 20, 22, 31].

314 Sanger sequencing was used to assess the genetic status of P2. Analysis found
315 homozygosity for MFN2 Arg334Lys, but only heterozygosity for FOXRED1 Ile485Asn. The family
316 also had an unaffected sister, for whom no genetic information was obtained.

317 Based on the genetic work-up from P1, we initially considered both MFN2 R334K and
318 FOXRED1 I485N variants. Given that the candidate variants in MFN2 and FOXRED1 have not
319 been described or characterized previously, we examined the conservation of the
320 corresponding amino acid changes in the protein. We found that the MFN2 R334 residue is
321 conserved in multiple species, including fruit flies and worms, as well as in the paralogous
322 protein MFN1, arguing that it plays an important role in protein function (Figure 1a).
323 Meanwhile, though the FOXRED1 I485 residue is conserved in vertebrates, it is not conserved in
324 earlier diverging metazoans such as flies or worms (Figure 1b). Upon subsequent sequencing of
325 P2, who was homozygous for MFN2 R334K, but only heterozygous for and FOXRED1 I485N, it
326 became evident that MFN2 R334K was most likely the causative variant for the remarkably
327 consistent phenotype in the two brothers. Topologically, the MFN2 R334K variant is near the
328 GTPase domain (Figure 1c), which is crucial for mitochondrial fusion [32].

329 **Characterization of patient fibroblasts harboring MFN2 R334K:**

330 As the candidate pathogenic variant in MFN2 is novel and has not been characterized
331 previously, fibroblasts from a skin biopsy of P1, who harboured homozygous MFN2 R334K and
332 FOXRED1 I485N variants, were obtained for functional analysis. We examined a variety of
333 cellular and mitochondrial phenotypes to see which, if any, might be consistent with MFN2
334 and/or FOXRED1 dysfunction. Unfortunately, fibroblast cells were not available for P2.

335 **Patient fibroblasts show evidence of mitochondrial dysfunction:**

336 Given the integral role of mitochondria in ATP production, we first assessed oxygen
337 consumption in patient fibroblasts, as this is a key indicator of changes to mitochondrial
338 function. Compared to control cells, we observed marked decreases in both basal (around half)
339 and maximal (around two-third) oxygen consumption (Figure 2a), as well as spare respiratory
340 capacity (Figure 2b). These findings are indicative of severely reduced mitochondrial respiration

341 in patient fibroblasts, consistent with an underlying mitochondrial dysfunction contributing to
342 the patient phenotype.

343 Next, we investigated the canonical function of MFN2 in mitochondrial fusion by
344 visualizing the mitochondrial network after immunofluorescent labeling for the mitochondrial
345 marker TOMM20 (Figure 2c). In comparison to the control fibroblasts, which showed elongated
346 and reticular mitochondrial network morphology, patient fibroblasts qualitatively displayed
347 more fragmented mitochondrial networks (Figure 2d). Quantitative analysis of the
348 mitochondrial networks confirmed patient fibroblasts had shorter mitochondria (Figure 2e).
349 Together, these findings are consistent with impaired mitochondrial fusion leading to more
350 fragmented mitochondria.

351 **Changes in mitochondrial nucleoids and mtDNA copy number depletion in patient fibroblasts:**

352 To provide further evidence of impaired mitochondrial fusion, we investigated the
353 distribution and abundance of mtDNA, which can be altered by impairments to mitochondrial
354 fusion, are linked to loss of MFN2 function, and have been observed for some MFN2 variants
355 [48, 56, 64]. Immunofluorescence imaging of mtDNA nucleoids (Figure 3a) revealed that the
356 patient fibroblasts exhibited approximately half as many nucleoids as control fibroblasts (Figure
357 3b), and that patient mtDNA nucleoids were smaller (Figure 3c). Consistent with the reduced
358 number of mtDNA nucleoids, we detected a 40% decrease in the mtDNA copy number in the
359 patient fibroblasts via qPCR (Figure 3d). Finally, we also investigated the presence of mtDNA
360 deletions, which are sometimes seen with MFN2 loss of function [64]. However, no mtDNA
361 deletions were detected (Figure 3e).

362 **Altered mito-ER contact sites and lipid droplet accumulation in patient fibroblasts:**

363 We investigated the size and abundance of mito-ER contact sites (MERCs) and lipid
364 droplets, as these phenotypes can be altered in fibroblasts from patient harboring pathogenic
365 MFN2 variants [30, 54]. As a proxy for MERCs, we utilized a proximity ligation assay (PLA) that
366 generates a fluorescent signal when mitochondria and ER are within ~40 nm (Figure 4a-b) [6].
367 Using confocal microscopy, we observed a decrease in the size and number of MERCs, which
368 was confirmed by quantitative analyses (Figure 4c-d). We examined lipid droplets by

369 immunofluorescence with the lipid droplet surface protein Perilipin 1 (Figure 5a). Compared to
370 control fibroblasts, we noted a distinct upregulation in the number (Figure 5b) and size (Figure
371 5c) of PLIN1 puncta in the R334K patient fibroblasts. These findings of decreased MERCs and
372 increased lipid droplets are consistent with previously reported alterations in fibroblasts from
373 patients with CMT2A harbouring MFN2 variants [9, 30].

374 **MFN2 and mitochondrial protein expression:**

375 As our findings were consistent with MFN2 dysfunction, we assessed if expression of
376 MFN2 and other mitochondrial proteins was impacted. While we did not observe changes in
377 MFN2 protein levels from total cell lysate (Figure 6a-b), we did observe a significant (~50%)
378 decrease in expression of the nuclear DNA encoded mitochondrial complex I subunit NDUFB8
379 (Figure 6a/c). Notably, there was no consistent significant change to the levels of the other
380 OXPHOS proteins investigated here, including mtDNA-encoded MTCO1. The cause for this
381 discrepancy in OxPhos protein expression is unknown, but likely does not reflect the mtDNA
382 depletion, which would be expected to cause a global decrease in OxPhos protein expression as
383 mtDNA encodes essential proteins for all the electron transport chain complexes except for
384 complex II.

385 **Complex I activity:**

386 Given the specific decrease in a Complex I protein, which is not typical of MFN2
387 dysfunction and likely not explained by mtDNA depletion, we wondered if the identified
388 FOXRED1 missense variant might also have functional consequences that could contribute to
389 the patient phenotype. As pathogenic defects in FOXRED1 are linked to dysfunction in complex
390 I assembly and stability, we also examined Complex I activity. Consistent with the reduced
391 protein expression, and possible complex I instability, we observed an ~50% reduction in
392 Complex I activity in patient fibroblasts (Figure 6d-e).

393 ***In vitro* re-expression of MFN2 R334K recapitulates Complex-I deficiencies**

394 To test if the reduced Complex I activity in patient fibroblasts can be explained by the
395 MFN2 R334K variant alone, we used a knockout re-expression system to test the pathogenicity

396 of the R334K MFN2 variant in a different genetic background. Using U2OS MFN2 KO cells, we
397 re-expressed either the WT MFN2 protein or the MFN2 R334K variant by viral transduction,
398 selecting cells expressing endogenous levels of MFN2 expression (Figure 7c-d). To confirm the
399 system recapitulates features of patient fibroblasts, we first looked at mitochondrial
400 morphology. As expected, MFN2 KO cells had severely fragmented mitochondrial networks,
401 which were rescued by re-expression of the WT protein in KO cells (Figure 7a-b). In line with the
402 mitochondrial fragmentation observed in patient fibroblasts, we found that MFN2 KO cells re-
403 expressing MFN2 R334K show partial rescue compared to MFN2 KO cells, but remained more
404 fragmented than control cells or KO cells re-expressing WT MFN2. Next, we examined the
405 expression of OxPhos proteins and Complex I function. MFN2 KO cells had severe reductions in
406 Complexes I, II, III, and IV subunits, which were fully rescued by re-expressing WT MFN2.
407 However, although Complex II, III and IV protein expression was rescued in MFN2 KO cells re-
408 expressing the R334K variant, Complex I protein expression was reduced by ~50% compared to
409 controls (Figure 7c-d). Looking at Complex I activity, MFN2 KO cells showed a marked reduction
410 that was fully rescued by WT MFN2. Although cells re-expressing MFN2 R334K showed a partial
411 rescue compared to the KO, there was still a significant 50% decrease compared to controls
412 (Figure 7e-f). Taken together, these findings confirm previous work showing MFN2 loss of
413 function can lead to reduced Complex I activity [34, 45], and demonstrate that the MFN2 R334K
414 variant alone can explain the 50% decrease in Complex I activity observed in patient fibroblasts.

415 ***In vivo* modelling of MFN2 R334K in *Drosophila melanogaster:***

416 To model the pathogenicity of the R334K MFN2 variant *in vivo*, we used a knockdown
417 re-expression paradigm in *Drosophila* (Figure 8a) that has been used to study the function of
418 other human MFN2 variants [19]. In this approach, depleting the MFN2 orthologue in flies,
419 *marf*, can be rescued by re-expressing WT human MFN2 (*hMFN2*). First, we examined the effect
420 of whole-body knockdown/re-expression using three different driver lines: Actin (*act5c*-Gal4),
421 Tubulin (*tub*-Gal4) or Daughterless (*da*-Gal4). Whole-body knockdown of *marf* was larval lethal
422 for all three promoters tested. While *act5c*-Gal4 and *tub*-Gal4 showed no survival, the weaker
423 *da*-Gal4 driver had ~10% survival (Figure 8b). Meanwhile, re-expression of WT *hMFN2* rescued
424 survival to ~60% (Figure 8b), confirming the ability of the WT human MFN2 to function in flies.

425 In contrast, re-expression of MFN2 R334K was insufficient to rescue the larval lethality (Figure
426 8b) in any of the whole-body driver lines.

427 Next, given the larval lethality of the whole-body *marf* knockdown and MFN2 R334K re-
428 expression, we used a tissue-specific drivers to examine the effects in neurons (*elav*-Gal4) and
429 cardiomyocytes (*tin*-Gal4), which are relevant to the neuromuscular patient pathology.
430 Knockdown of *marf* in cardiomyocytes showed no significant lethality (Figure 8c). Next, we
431 assayed for locomotor function using a negative geotaxis climbing assay. We observed a
432 marked decrease in climbing ability of flies with knockdown of *marf*, which is nearly completely
433 rescued by re-expressing WT MFN2, but not by re-expression of MFN2 R334K (Figure 8d). Using
434 the neuronal driver, we saw 70% survival with *marf* knockdown, which was completely rescued
435 with WT MFN2, while MFN2 R334K had 95% survival (Figure 8e). In terms of climbing ability
436 with the neuron driver line *marf* knockdown also led to a significant decrease, which was
437 completely rescued by WT MFN2 climbing. In contrast, MFN2 R334K provided only a slight
438 rescue (Figure 8f). Importantly, we confirmed similar levels of WT MFN2 and MFN2 R334K in
439 our fly lines (Figure 8g). Overall, these data show that the MFN2 R334K variant has reduced
440 functionality and is unable to rescue *marf* knockdown *in vivo* to the same level as WT MFN2.
441 Moreover, the deficits seen with neuronal and cardiomyocyte-specific knockdown, reflect the
442 severe pathology seen in the patient.

443 **Pharmacologic ISR activation rescues MFN2 R334K dysfunction in patient cells**

444 Given our previous work showing ISR activation rescues mitochondrial fragmentation
445 and oxygen consumption in MFN2-deficient cells [5, 8], we speculated that ISR activation would
446 ameliorate dysfunction in MFN2 R334K patient fibroblasts. To this end, a 6-hour treatment with
447 three distinct ISR activators (Halofuginone, 3610, and Parogrelil) completely rescued
448 mitochondrial morphology in R334K patient fibroblasts (Figure 9a-b/Supplemental Figure 1a-d).
449 Furthermore, all three ISR activators also partially rescued OCR deficits (Figure 9c). Importantly,
450 co-treatment with the ISR inhibitor ISRIB prevented the rescue of both morphology and OCR for
451 all three compounds, confirming that this rescue is dependent on ISR activation, rather than
452 any potential off-target effects of the drugs. Overall, these findings show that pharmacological

453 ISR activation is beneficial for MFN2 dysfunction, even for severe perturbations such as those
454 caused by MFN2 R334K.

455 **Discussion:**

456 We report two siblings who presented with severe hypotonia, areflexia and limited
457 movement upon birth, who both harboured a novel homozygous single missense variant in
458 MFN2 p.(Arg334Lys). We speculate the location of the R334K MFN2 variant is crucial for proper
459 protein function, possibly by altering the nearby GTPase domain of the protein. Though CMT2A
460 can be an early-onset disease that can eventually restrict patient movement as the disease
461 progresses, the patients reported here exhibited lack of movement upon birth, indicative of a
462 more severe disease onset. Moreover, both patients succumbed in infancy (<6 weeks). Though
463 areflexia and hypotonia phenotypes are not typical of CMT2A, there are a few previous reports
464 of both these phenotypes in patients harbouring MFN2 variants with severe early onset disease
465 prognosis [35, 43, 48, 51, 57, 65]. However, the patients we report here presented with
466 symptoms immediately upon birth, as opposed to the examples in the previous reports, where
467 symptoms presented from 6-12 months. With respect to the early onset of severe phenotypes
468 linked to MFN2 dysfunction, there is a recent report of a patient with severe CNS complications
469 who harboured a homozygous 50 amino acid deletion in MFN2 with antenatal presentation
470 that resulted in pregnancy termination at 31 weeks [13]. In this regard, the fact that loss of
471 MFN2 function leads to embryonic lethality in mice [12] and larval lethality in fruit flies [19], is
472 consistent with a severe loss of MFN2 function due to the R334K variant.

473 In support of the notion that the R334K variant impairs MFN2 functions, we observed
474 changes across all the functions we explored, including mitochondrial network morphology,
475 oxidative phosphorylation, complex I activity, MERCs, mtDNA copy number and nucleoids, as
476 well as cellular lipid droplets. These findings suggest that the novel R334K variant causes severe
477 dysfunction of the MFN2 protein. To our knowledge, there are no previously characterized
478 MFN2 CMT2a variants with defects across all these functions [64]. However, to some degree
479 this finding likely reflects the fact that few MFN2 variants have been characterized extensively
480 for their impact on MFN2 functions, highlighting our limited understanding of how MNF2

481 variants impact MFN2 functions. In terms of MFN2 variants associated with more severe
482 cellular phenotypes, it is notable that MFN2 variants that correlate with reduced mtDNA copy
483 number and impaired oxidative phosphorylation are reported in patients that tend to present
484 with earlier-onset and severe clinical outcomes [33, 54, 60]. Collectively, this evidence is
485 consistent with severe MFN2 dysfunction contributing to the very early onset of clinical
486 symptoms in the patients we report here.

487 In light of the additional homozygous FOXRED1 variant in P1, it is also worth briefly
488 discussing the 50% Complex I deficiency in the fibroblasts from this patient, which is not typical
489 of pathogenic MFN2 variants. Notably, complete loss of MFN2 function can lead to a specific
490 deficit in Complex I expression and function [34], which we also observe in U2OS KO cells.
491 Moreover, Complex I dysfunction was also reported with the MFN2 variant harbouring a 50
492 amino acid deletion resulting in pregnancy termination [13]. Thus, MFN2 dysfunction alone is
493 sufficient to cause Complex I deficiency. Though FOXRED1 is a molecular chaperone that is
494 important for the assembly of mitochondrial complex I [22, 42], several lines of evidence argue
495 against a potential role for the FOXRED1 I485N variant contributing to the phenotype of the
496 patients. First, the patient phenotypes do not match. Homozygous or compound heterozygous
497 recessive FOXRED1 variants cause mitochondrial complex I deficiency, nuclear type 19
498 (MC1DN19), where only a handful of cases have been described [4, 11, 20, 22, 24, 27, 66].
499 Clinical phenotypes of MC1DN19 mimic common mitochondrial disorders such as Leigh
500 syndrome and mitochondrial encephalopathy [11, 27, 36], including lactic acidosis and growth
501 restrictions. In contrast, there was no evidence of lactic acidosis in P1 or P2. Meanwhile, though
502 MC1DN19 patients can have hypotonia [20, 27], and can also be diagnosed with restricted
503 movement accompanying Leigh syndrome [22], there are no reports of areflexia in FOXRED1
504 patients, who typically survive well past infancy [4]. Secondly, the genetics also argue against
505 I485N FOXRED1 variant contributing to pathology, as FOXRED1 is autosomal recessive, while P2
506 was heterozygous for the I485N FOXRED1 variant. Thus, despite the fact that novel I485N
507 FOXRED1 variant reported here is located at the C-terminus of the protein, similar to other
508 pathogenic FOXRED1 variants described to date, and the fact that FOXRED1 patient fibroblasts
509 also have reduced Complex I activity [20] (with patient myoblasts reported with deficiencies in

510 both Complex I and Complex II [66]), this variant was ruled out as a contributing factor for the
511 phenotype of P1 and P2, who had identical presentations. Finally, our results in MFN2 KO cells
512 re-expressing the R334K variant show that this variant alone is sufficient to cause a 50%
513 decrease in Complex I activity, fully explaining the loss of Complex I activity in patient
514 fibroblasts.

515 As there is no cure for CMT2A or other MFN2-mediated pathology, it is notable that
516 pharmacological ISR activation ameliorates the dysfunctions tied to mitochondrial
517 fragmentation and impaired oxygen consumption in MFN2 R334K patient cells. Notably, one of
518 the ISR activators we tested, Parogrelil, is an FDA-approved drug that has passed phase I clinical
519 trials [26, 28]. However, before clinical use for MFN2 pathology, further work is needed to
520 decipher mechanisms of ISR-dependent rescue, benefits beyond cultured cells, as well as
521 temporal and dosage effects. Nonetheless, ISR activation is a promising therapeutic
522 intervention for MFN2-mediated pathology.

523 Rapid whole exome sequencing (WES) has repeatedly shown that a quicker time to
524 diagnosis guides goals of clinical care, including less failed treatments, and ultimately lowers
525 the financial burden on the health care system [14, 23, 37]. While previous reports suggests
526 that between 30-50% of WES cases are solved or partly solved by a known disease-associated
527 gene, additional cases may reveal novel genes of uncertain significance (GUS). This study
528 demonstrates the utility of rapid WES accompanied by functional experiments to assess these
529 GUS and provide a diagnosis. Functional studies also have the potential to discover new
530 treatment options for novel genes. However, as this study demonstrates, this is dependent
531 upon the damaging effects of the variant on the normal function of the gene and/or protein.
532 Regardless, this study demonstrates the value of collaboration between clinical and research
533 colleagues.

534 While we acknowledge the limitations of studying a novel protein variant in a single
535 family, our functional studies in cells (both patient fibroblasts and MFN2 KO cells re-expressing
536 the R334K variant), and in an animal model clearly demonstrate that functional impairment of
537 the R334K MFN2 variant is sufficient to explain the observed cellular and patient phenotypes.

538 The fact that that U2OS cells re-expressing the R334K variant recapitulates the key cellular
539 phenotypes of mitochondrial fragmentation and reduced oxygen consumption show that this
540 variant, rather than the FOXRED1 variant or some other undetected variant, is responsible for
541 the observed mitochondrial dysfunction in patient fibroblasts. Meanwhile, modeling of the
542 R334K variant in *Drosophila* provides *in vivo* evidence that the R334K variant can explain the
543 severe early onset patient phenotypes. Thus, combined with clear genetic evidence, this
544 functional work strongly argues for R334K as a novel pathogenic MFN2 variant causing a severe
545 early onset pathology. This work also highlights the fact that MFN2 dysfunction can cause much
546 more severe pathology than CMT2A typically recognized to be associated with MFN2 variants.

547

548 **Acknowledgements**

549 The authors would like to thank the study participants and their family. We would also
550 like to thank Matthew Lines for his input on the manuscript. We would like to thank Dr. Paul
551 Marcogliese (University of Manitoba, Canada) for his expertise and technical guidance with the
552 *Drosophila* work.

553

554 **Conflict of Interests**

555 The authors declare that they have no conflict of interest.

556

557 **Author contributions**

558 Designed and/or performed and analyzed mitochondrial or *Drosophila* experiments, MZ,
559 CC, SG, RLW and TES; Clinical evaluation of patients and write up, JLM, BM, AMI, FPB; Analyzed
560 exome data AVP; Drafted the manuscript or figures, MZ, AVP, BM, TES. All authors discussed
561 the results and commented on the manuscript.

562

563 **Funding**

564 This work was supported by funds provided by the Canadian Institutes of Health
565 Research (TES) and the Alberta Children's Hospital Research Institute (Owerko Center) (MZ). MZ

566 was supported by a Hotchkiss Brain Institute International Recruitment Scholarship. The
567 funders had no role in study design, data collection and interpretation, or the decision to
568 submit the work for publication.

569 **Figure Legends:**

570

571 Figure 1: The MFN2 and FOXRED1 single nucleotide variants are conserved across species. (a)
572 Multiple sequence alignment data shows conservation of MFN2 at Arginine-334 and (b)
573 FOXRED1 conservation of Isoleucine 485. Accession numbers used for comparison are: MFN2:
574 O95140-1; O95140-2; MFN1: Q8IWA4; Mouse MFN2: Q80U63; Fish MFN2: A8WIN6; Fly MFN2:
575 Q7YU24; Worm MFN2: Q23424; FXRD1: Q96CU9; FXRD1 [2]: Q96CU9-2; FXRD1 [3]: Q96CU9-3;
576 Mouse FXRD1: Q3TQB2; Fish FXRD1: A0A0R4IHD6; Fly FXRD1: Q9VJ10; Worm FXRD1:
577 A0A0V1BI76. (c) Topological representation of Mitofusin 2, highlighting the position of MFN2
578 R334K on the GTPase domain.

579

580 Figure 2: MFN2 R334K leads to severe mitochondrial dysfunction: (a) SeaHorse Oxygen
581 Consumption Rate (OCR) indicating control and patient fibroblasts, measured using XF23
582 extracellular flux analyzer (2 biological replicates with 12 technical replicates). The error bars on
583 the graph indicate the mean OCR +/ SD. (b) Quantification of spare respiratory capacity in
584 control fibroblasts and patient fibroblasts (2 biological replicates with 12 technical replicates);
585 the bars indicate mean +/- SD, statistics are from an unpaired t-test. (c) Representative STED
586 confocal microscopy images showing mitochondrial network morphology in control vs MFN2
587 R334K patient fibroblasts, stained using anti-TOMM20. (d)Graphical representation of
588 qualitative analysis of mitochondrial branch appearance (fused/intermediate/fragmented),
589 from analysis of 150 images including 3 biological replicates, the bars indicate mean for each
590 category +/ SD, statistics are from an unpaired t-test. (e) Violin plot showing quantitative
591 analyses of mean mitochondrial branch length in control and patient fibroblasts (from 150 cells
592 including 3 biological replicates), with violin plots indicating median and interquartile range
593 (IQR), from an unpaired t-test. Statistical values indicate the following: ns $P > 0.05$, * $P \leq 0.05$,
594 **** $P \leq 0.0001$.

595

596 Figure 3: Alterations to mitochondrial DNA in patient fibroblasts. (a) Representative confocal
597 images showing DAPI (nucleus) and mitochondrial nucleoids (anti-dsDNA) co-localized with the
598 mitochondrial network (anti-TOMM20) for control (top panels) and patient fibroblasts (bottom
599 panels). (b) Quantitative analyses of number of mitochondrial nucleoids per cell in control and
600 patient fibroblasts, the colors indicate biological replicates, the lines indicate mean number of
601 mito-nucleoids per cell +/ SD, statistics are from an unpaired t-test. (c) Quantitative analyses of
602 average size(s) of mitochondrial nucleoids in control and patient fibroblasts, the colors indicate
603 biological replicates, with the lines showing mean +/ SD, statistics are from an unpaired t-test.
604 (d) Quantitative analysis of mtDNA copy number in control and patient fibroblasts, relative to
605 18S rDNA, the colors indicate biological replicates, bars indicate mean +/ SD, statistics are from
606 an unpaired t-test. (e) Representative image of agarose gel to detect mtDNA deletions using
607 0.6% agarose gel following long-range PCR to target mtDNA amplification and ladder shown on
608 the left. Statistics shown on the graph represent: ns $P > 0.05$, * $P \leq 0.05$, ** $P \leq 0.01$, **** $P \leq$
609 0.0001.

610

611 Figure 4: Changes to mito-ER contact sites in patient fibroblasts. (a) Top panel shows
612 representative confocal images of mitochondria (anti-TOMM20) and ER (anti-calnexin) co-
613 localization, MERCs (PLA probes) and merged images for control fibroblasts. The bottom panel
614 shows zoomed representation of boxed region. (b) Top panel shows representative confocal
615 images of mitochondria (anti-TOMM20) and ER (anti-calnexin) co-localization, MERCs (PLA
616 probes) and merged images for patient fibroblasts. The bottom panel shows zoomed
617 representation of boxed region. (c) Quantitative analyses of number of PLA signals (MERCs) per
618 cell in control and patient fibroblasts, colors indicate biological replicates, the violin plots show
619 distribution of data, while the lines indicate mean +/ SD, statistics are from an unpaired t-test.
620 (d) Quantitative analyses of average size(s) of PLA puncta (size of MERCs) in control and patient
621 fibroblasts bars indicate the mean size of PLA puncta +/ SD, statistics are from an unpaired t-
622 test. Statistics used in the graphs represent the following*** $P \leq 0.001$, **** $P \leq 0.0001$.

623

624 Figure 5: Changes to cellular lipid droplet accumulation in control and patient fibroblasts. (a)
625 Representative confocal images from control (top) and patient (bottom) fibroblasts stained for
626 lipid droplets using anti-PLIN1 antibody. (b) Quantification of mean lipid droplet number per
627 cell in control and patient fibroblasts using anti-PLIN1, colors indicate biological replicates, bars
628 indicate mean +/ SD, statistics are from an unpaired t-test. (c) Quantification of mean lipid
629 droplet size in control and patient fibroblasts using anti-PLIN1, colors indicate biological
630 replicates, lines indicate mean +/ SD, ; violin shows distribution of data, statistics are from an
631 unpaired t-test. The statistics shown are represented by: **** $P \leq 0.0001$.

632

633 Figure 6: MFN2 R334K impedes levels and activity of OXPHOS Complex-I. (a) Representative
634 Western Blot images from control and MFN2 R334K patient fibroblasts showing protein levels
635 of MFN2 and the OxPhos complexes, as well as loading control Beta-Actin and mitochondrial
636 loading control HSP-60. (b) Quantification of MFN2 levels in control fibroblasts and patient
637 fibroblasts relative to Beta-Actin, colours indicate biological replicates, the bars indicate mean
638 levels of MFN2 +/ SD, statistics show an unpaired t-test. (c) Quantification of mitochondrial
639 OxPhos complexes (I-V) levels from Western Blot analyses in control and patient fibroblasts
640 normalized to cellular beta-actin levels, colours indicate biological replicates, the lines indicate
641 mean for each category mean +/ SD, statistics are from individual unpaired t-tests versus the
642 control. (d) Representative images showing dipsticks used to characterize relative complex I
643 activity in control and patient fibroblasts, using the complex I dipstick assay. (e) Quantification
644 of relative complex-I activity performed using complex-I dipstick assay in control and patient
645 fibroblasts, colours indicate biological replicates, while bars indicate mean for each category +/
646 SD, Statistics shown indicate: ns $P > 0.05$, *** $P \leq 0.001$, **** $P \leq 0.0001$.

647

648 Figure 7- *In vitro* modelling of MFN2 R334K shows failure to rescue mitochondrial
649 fragmentation and complex-I deficiencies. (a) Representative confocal images showing
650 mitochondrial network morphology, labelled using anti-TOMM20 antibody for WT U2OS, U2OS
651 MFN2 KO and re-expression of WT MFN2 or MFN2 R334K in KO cells. (b) Quantitative analyses

652 of mitochondrial network morphology represented by mean mitochondrial branch length,
653 colours indicate biological replicates, violins plots show the median branch length and inter-
654 quartile range, statistics were performed using a one-way ANOVA. (c) Representative western
655 blot images showing re-expression levels of MFN2 (WT/R334K) and corresponding levels of
656 OXPHOS complex subunits, as well as loading control beta-actin. (d) Quantitative analyses in
657 WT U2OS/MFN2 KO/WT re-expression/MFN2 R334K re-expression in KO cells showing levels of
658 proteins (MFN2 re-expression levels and OXPHOS complexes); the colours indicate biological
659 replicates, bars show the mean protein levels +/- SD, statistics are from an unpaired t-test. (e-f)
660 Complex-I dysfunction in U2OS MFN2 R334K re-expression cells with (e) representative images
661 showing complex-I activity dipsticks and (f) Quantitative analyses of complex-I dipstick assay,
662 the colours indicate biological replicates, the lines show mean complex I activity +/- SD,
663 statistics are from one-way ANOVA. The statistics represent the following: ns $P > 0.05$, ** $P \leq$
664 0.01, **** $P \leq 0.0001$.

665

666 Figure 8: In vivo analyses of MFN2 R334K using *Drosophila melanogaster* show lethality and
667 locomotor dysfunctions. (a) Schematic representing Gal4-UAS approach for human disease
668 modelling in *Drosophila melanogaster*, with Gal4 under the control of whole body/tissue
669 specific promoters leading to expression of UAS-hMFN2 on chromosome II (phiC31 integrase
670 approach) and UAS-*marf* RNAi on chromosome III. UAS-*mCherry* RNAi was used as a control for
671 the Gal4-UAS system. (b) Whole-body survival assay in control, *marf* knockdown and re-
672 expression of hMFN2 WT and MFN2 R334K fly lines using Actin (*act5c*-Gal4*)*, Tubulin (*tub*-Gal4)
673 and Daughterless (*da*-Gal4) driver lines. n=80 flies, with four independent replicates. Bars show
674 mean survivability +/- SD, statistics are from unpaired t-tests. (c) Tissue-specific survival assay
675 for cardiomyocytes, using control, *marf* knockdown and re-expression of hMFN2 WT and MFN2
676 R334K fly lines using tinman (*tin*-Gal4) driver line. n=80, with four independent replicates; The
677 bars on the graph show mean survival +/- SD, statistics are from unpaired t-tests. (d) Negative
678 geotaxis assay to look for climbing ability of flies with changes to cardiomyocytes *(tin)*
679 knockdown and re-expression of human MFN2, lines show mean +/- SD, statistics are from
680 unpaired t-tests at each time point for WT-re=expression vs R334K re-expression. (e) Tissue-

681 specific survival assay for neurons, using control, *marf* knockdown and re-expression of hMFN2
682 WT and MFN2 R334K fly lines using elav (*elav*-Gal4) driver line. n=80, with four independent
683 replicates; The bars on the graph show mean survival +/- SD, statistics are from unpaired t-
684 tests. (f) Negative geotaxis assay to look for climbing ability of flies with changes to neurons
685 *(elav)* knockdown and re-expression of human MFN2, lines show mean +/- SD, statistics are
686 from unpaired t-tests at each time point for WT-re-expression vs R334K re-expression.
687 (f)Representative Western Blot images showing expression of human MFN2 protein expression
688 in in control, *marf* knockdown and re-expression of hMFN2 WT and MFN2 R334K fly lines under
689 the control of *elav*-Gal4. (b) Statistics represent the followingns $P > 0.05$, * $P \leq 0.05$, ** $P \leq 0.01$,
690 **** $P \leq 0.0001$.

691

692 Figure 9: ISR activation rescues mitochondrial fragmentation and boosts cellular oxygen
693 consumption in MFN2 R334K patient cells. (a) Representative confocal images showing
694 mitochondrial network morphology using MitoTracker green for control fibroblasts vs MFN2
695 R334K patient fibroblasts treated with ISR activators/inhibitors for 6 hours with vehicle, #3610
696 (10uM), Parogrelil (10uM) and Halofuginone (100nM), along with ISRIB (200nM). (b)
697 Quantitative analyses of mitochondrial network morphology for control/patient fibroblasts
698 treated with ISR activators, points on the graph indicate biological replicates, lines show mean
699 mitochondrial branch length +/- SD, statistics come from one-way ANOVA. (c) Quantitative
700 analyses of cellular oxygen consumption rate measured using Resipher OCR, for control
701 fibroblasts and patient fibroblasts treated for 6 hours with vehicle, #3610 (10uM), Parogrelil
702 (10uM) and Halofuginone (100nM), along with ISRIB (200nM). Colours indicate biological
703 replicates, violin plots show the median OCR and IQR, one-way ANOVA. Statistics on the graphs
704 represent the following: ns $P > 0.05$, * $P \leq 0.05$, **** $P \leq 0.0001$.

705

706 Supplemental Figure S1: ISR activation rescues mitochondrial fragmentation and boosts cellular
707 oxygen consumption. (A) Representative confocal images showing mitochondrial network
708 morphology using MitoTracker green for control fibroblasts treated with the following ISR

709 activators/inhibitors for 6 hours with vehicle, #3610 (10uM), Parogrelil (10uM) and
710 Halofuginone (100nM), along with ISRIB (200nM). (b) Quantitative analyses of mitochondrial
711 network morphology for control fibroblasts treated with ISR activators, points indicate
712 biological replicates, bars show mean +/- SD, statistics represent a one-way ANOVA. (c)
713 Representative confocal images showing mitochondrial network morphology using MitoTracker
714 green for MFN2 R334K patient fibroblasts treated with ISR activators/inhibitors for 6 hours with
715 vehicle, #3610 (10uM), Parogrelil (10uM) and Halofuginone (100nM), along with ISRIB (200nM).
716 (d) Quantitative analyses of mitochondrial network morphology for patient fibroblasts, colours
717 indicate biological replicates, symbols indicate means of biological replicates, lines show mean
718 +/- SD, one-way ANOVA. (e) Quantitative analyses of cellular oxygen consumption rate
719 measured using Resipher OCR, for control fibroblasts and patient fibroblasts treated for 6 hours
720 with vehicle, #3610 (10uM), Parogrelil (10uM) and Halofuginone (100nM), along with ISRIB
721 (200nM). Colours indicate biological replicates, violin plots show median and IQR, statistics
722 represent a one-way ANOVA. Statistical symbols represent ns $P > 0.05$, * $P \leq 0.05$, **** $P \leq$
723 0.0001.

724

725 **References:**

726 1. Ainbinder A, Boncompagni S, Protasi F, Dirksen RT (2015) Role of Mitofusin-2 in mitochondrial
727 localization and calcium uptake in skeletal muscle. Cell Calcium 57:14–24. doi:
728 10.1016/j.ceca.2014.11.002

729 2. Amiott EA, Lott P, Soto J, Kang PB, McCaffery JM, DiMauro S, Abel ED, Flanigan KM, Lawson VH,
730 Shaw JM (2008) Mitochondrial fusion and function in Charcot-Marie-Tooth type 2A patient
731 fibroblasts with mitofusin 2 mutations. Exp Neurol 211:115–127. doi:
732 10.1016/j.expneurol.2008.01.010

733 3. Anderson NS, Haynes CM (2020) Folding the Mitochondrial UPR into the Integrated Stress
734 Response. Trends Cell Biol 30:428–439. doi: 10.1016/j.tcb.2020.03.001

735 4. Apatean D, Rakic B, Brunel-Guitton C, Hendson G, Bai R, Sargent MA, Lavoie PM, Patel M, Stockler-
736 Ipsiroglu S (2019) Congenital lactic acidosis, cerebral cysts and pulmonary hypertension in an
737 infant with FOXRED1 related complex I deficiency. Mol Genet Metab Rep 18:32–38. doi:
738 10.1016/j.ymgmr.2018.12.006

739 5. Baron KR, Oviedo S, Krasny S, Zaman M, Aldakhlallah R, Mathur P, Pfeffer G, Bollong MJ, Shutt T,
740 Grotjahn DA, Wiseman RL (2024) Pharmacologic Activation of Integrated Stress Response Kinases
741 Inhibits Pathologic Mitochondrial Fragmentation. eLife 13. doi: 10.7554/eLife.100541.1

742 6. Benhammouda S, Vishwakarma A, Gatti P, Germain M (2021) Mitochondria Endoplasmic
743 Reticulum Contact Sites (MERCs): Proximity Ligation Assay as a Tool to Study Organelle Interaction.
744 Front Cell Dev Biol 9:789959. doi: 10.3389/fcell.2021.789959

745 7. Bombelli F, Stojkovic T, Dubourg O, Echaniz-Laguna A, Tardieu S, Larcher K, Amati-Bonneau P,
746 Latour P, Vignal O, Cazeneuve C, Brice A, Leguern E (2014) Charcot-Marie-Tooth Disease Type 2A:
747 From Typical to Rare Phenotypic and Genotypic Features. JAMA Neurology 71:1036–1042. doi:
748 10.1001/jamaneurol.2014.629

749 8. Bora P, Zaman M, Oviedo S, Kutseikin S, Madrazo N, Mathur P, Pannikkat M, Krasny S, Chu A,
750 Johnson KA, Grotjahn DA, Shutt TE, Wiseman RL (2025) Drug Repurposing Screen Identifies an HRI
751 Activating Compound that Promotes Adaptive Mitochondrial Remodeling in MFN2-deficient Cells.
752 2025.06.23.660251

753 9. Boutant M, Kulkarni SS, Joffraud M, Ratajczak J, Valera-Alberni M, Combe R, Zorzano A, Cantó C
754 (2017) Mfn2 is critical for brown adipose tissue thermogenic function. EMBO J 36:1543–1558. doi:
755 10.15252/embj.201694914

756 10. de Brito OM, Scorrano L (2008) Mitofusin 2 tethers endoplasmic reticulum to mitochondria. Nature
757 456:605–610. doi: 10.1038/nature07534

758 11. Calvo SE, Tucker EJ, Compton AG, Kirby DM, Crawford G, Burtt NP, Rivas M, Guiducci C, Bruno DL,
759 Goldberger OA, Redman MC, Wiltshire E, Wilson CJ, Altshuler D, Gabriel SB, Daly MJ, Thorburn DR,
760 Mootha VK (2010) High-throughput, pooled sequencing identifies mutations in NUBPL and
761 FOXRED1 in human complex I deficiency. Nat Genet 42:851–858. doi: 10.1038/ng.659

762 12. Chen H, Detmer SA, Ewald AJ, Griffin EE, Fraser SE, Chan DC (2003) Mitofusins Mfn1 and Mfn2
763 coordinately regulate mitochondrial fusion and are essential for embryonic development. J Cell
764 Biol 160:189–200. doi: 10.1083/jcb.200211046

765 13. Chevrollier A, Bonnard AA, Ruaud L, Gueguen N, Perrin L, Desquiret-Dumas V, Guimiot F, Becker P-
766 H, Levy J, Reynier P, Gaignard P (2024) Homozygous MFN2 variants causing severe antenatal
767 encephalopathy with clumped mitochondria. Brain 147:91–99. doi: 10.1093/brain/awad347

768 14. Chung CCY, Leung GKC, Mak CCY, Fung JLF, Lee M, Pei SLC, Yu MHC, Hui VCC, Chan JCK, Chau JFT,
769 Chan MCY, Tsang MHY, Wong WHS, Tung JYL, Lun KS, Ng YK, Fung CW, Wong MSC, Wong RMS, Lau
770 YL, Chan GCF, Lee SL, Yeung KS, Chung BHY (2020) Rapid whole-exome sequencing facilitates
771 precision medicine in paediatric rare disease patients and reduces healthcare costs. Lancet Reg
772 Health West Pac 1:100001. doi: 10.1016/j.lanwpc.2020.100001

773 15. Chung KW (2006) Early onset severe and late-onset mild Charcot-Marie-Tooth disease with
774 mitofusin 2 (MFN2) mutations. Brain 129:2103–2118. doi: 10.1093/brain/awl174

775 16. Detmer SA, Chan DC (2007) Complementation between mouse Mfn1 and Mfn2 protects
776 mitochondrial fusion defects caused by CMT2A disease mutations. J Cell Biol 176:405–414. doi:
777 10.1083/jcb.200611080

778 17. Di Tommaso P, Moretti S, Xenarios I, Orobitg M, Montanyola A, Chang J-M, Taly J-F, Notredame C
779 (2011) T-Coffee: a web server for the multiple sequence alignment of protein and RNA sequences
780 using structural information and homology extension. Nucleic Acids Res 39:W13-17. doi:
781 10.1093/nar/gkr245

782 18. Eaton JS, Lin ZP, Sartorelli AC, Bonawitz ND, Shadel GS (2007) Ataxia-telangiectasia mutated kinase
783 regulates ribonucleotide reductase and mitochondrial homeostasis. J Clin Invest 117:2723–2734.
784 doi: 10.1172/JCI31604

785 19. Eschenbacher WH, Song M, Chen Y, Bhandari P, Zhao P, Jowdy CC, Engelhard JT, Dorn GW (2012)
786 Two rare human mitofusin 2 mutations alter mitochondrial dynamics and induce retinal and
787 cardiac pathology in Drosophila. PLoS One 7:e44296. doi: 10.1371/journal.pone.0044296

788 20. Fassone E, Duncan AJ, Taanman J-W, Pagnamenta AT, Sadowski MI, Holand T, Qasim W, Rutland P,
789 Calvo SE, Mootha VK, Bitner-Glindzicz M, Rahman S (2010) FOXRED1, encoding an FAD-dependent
790 oxidoreductase complex-I-specific molecular chaperone, is mutated in infantile-onset
791 mitochondrial encephalopathy. Hum Mol Genet 19:4837–4847. doi: 10.1093/hmg/ddq414

792 21. Feely SME, Laura M, Siskind CE, Sottile S, Davis M, Gibbons VS, Reilly MM, Shy ME (2011) MFN2
793 mutations cause severe phenotypes in most patients with CMT2A. Neurology 76:1690–1696. doi:
794 10.1212/WNL.0b013e31821a441e

795 22. Formosa LE, Mimaki M, Frazier AE, McKenzie M, Stait TL, Thorburn DR, Stroud DA, Ryan MT (2015)
796 Characterization of mitochondrial FOXRED1 in the assembly of respiratory chain complex I. Hum
797 Mol Genet 24:2952–2965. doi: 10.1093/hmg/ddv058

798 23. Freed AS, Clowes Candadai SV, Sikes MC, Thies J, Byers HM, Dines JN, Ndugga-Kabuye MK, Smith
799 MB, Fogus K, Mefford HC, Lam C, Adam MP, Sun A, McGuire JK, DiGeronimo R, Dipple KM, Deutsch

800 GH, Billimoria ZC, Bennett JT (2020) The Impact of Rapid Exome Sequencing on Medical
801 Management of Critically Ill Children. J Pediatr 226:202-212.e1. doi: 10.1016/j.jpeds.2020.06.020

802 24. Haack TB, Madignier F, Herzer M, Lamantea E, Danhauser K, Invernizzi F, Koch J, Freitag M, Drost R,
803 Hillier I, Haberberger B, Mayr JA, Ahting U, Tiranti V, Rötig A, Iuso A, Horvath R, Tesarova M, Baric
804 I, Uziel G, Rolinski B, Sperl W, Meitinger T, Zeviani M, Freisinger P, Prokisch H (2012) Mutation
805 screening of 75 candidate genes in 152 complex I deficiency cases identifies pathogenic variants in
806 16 genes including NDUFB9. J Med Genet 49:83–89. doi: 10.1136/jmedgenet-2011-100577

807 25. Hikiami R, Yamashita H, Koita N, Jingami N, Sawamoto N, Furukawa K, Kawai H, Terashima T, Oka
808 N, Hashiguchi A, Takashima H, Urushitani M, Takahashi R (2018) Charcot-Marie-Tooth disease type
809 2A with an autosomal-recessive inheritance: the first report of an adult-onset disease. J Hum
810 Genet 63:89–92. doi: 10.1038/s10038-017-0353-3

811 26. Hori M, Iwama T, Asakura Y, Kawanishi M, Kamon J, Hoshino A, Takahashi S, Takahashi K, Nakaike
812 S, Tsuruzoe N (2009) NT-702 (parogrelil hydrochloride, NM-702), a novel and potent
813 phosphodiesterase 3 inhibitor, suppress the asthmatic response in guinea pigs, with both
814 bronchodilating and anti-inflammatory effects. Eur J Pharmacol 618:63–69. doi:
815 10.1016/j.ejphar.2009.07.005

816 27. Hu C, Xu Q, Shen J, Wang Y (2021) Clinical and Genetic Characteristics of Mitochondrial
817 Encephalopathy Due to FOXRED1 Mutations: Two Chinese Case Reports and a Review of the
818 Literature. Front Neurol 12:633397. doi: 10.3389/fneur.2021.633397

819 28. Ishiwata N, Noguchi K, Kawanishi M, Asakura Y, Hori M, Mitani A, Ito Y, Takahashi K, Nishiyama H,
820 Shudo N, Takahashi S, Takahashi K, Tsuruzoe N, Nakaike S (2007) NT-702 (parogrelil hydrochloride,
821 NM-702), a novel and potent phosphodiesterase inhibitor, improves reduced walking distance and
822 lowered hindlimb plantar surface temperature in a rat experimental intermittent claudication
823 model. Life Sci 81:970–978. doi: 10.1016/j.lfs.2007.07.025

824 29. Kimura Y, Nishikawa A, Hashiguchi A, Etoh M, Yoshimura A, Asai K, Miyashita N, Takashima H, Sumi
825 H, Naka T (2022) An MFN2-related Charcot-Marie-Tooth Disease Patient with Optic Nerve Atrophy,
826 Neurogenic Bladder Dysfunction, and Diaphragmatic Weakness. Intern Med 61:1743–1747. doi:
827 10.2169/internalmedicine.6487-20

828 30. Larrea D, Pera M, Gonnelli A, Quintana-Cabrera R, Akman HO, Guardia-Laguarta C, Velasco KR,
829 Area-Gomez E, Dal Bello F, De Stefani D, Horvath R, Shy ME, Schon EA, Giacomello M (2019) MFN2
830 mutations in Charcot-Marie-Tooth disease alter mitochondria-associated ER membrane function
831 but do not impair bioenergetics. Hum Mol Genet 28:1782–1800. doi: 10.1093/hmg/ddz008

832 31. Lemire BD (2015) Evolution of FOXRED1, an FAD-dependent oxidoreductase necessary for
833 NADH:ubiquinone oxidoreductase (Complex I) assembly. Biochim Biophys Acta 1847:451–457. doi:
834 10.1016/j.bbabio.2015.01.014

835 32. Li Y-J, Cao Y-L, Feng J-X, Qi Y, Meng S, Yang J-F, Zhong Y-T, Kang S, Chen X, Lan L, Luo L, Yu B, Chen
836 S, Chan DC, Hu J, Gao S (2019) Structural insights of human mitofusin-2 into mitochondrial fusion
837 and CMT2A onset. Nat Commun 10:4914. doi: 10.1038/s41467-019-12912-0

838 33. Loiseau D, Chevrollier A, Verny C, Guillet V, Gueguen N, Pou de Crescenzo M-A, Ferré M, Malinge
839 M-C, Guichet A, Nicolas G, Amati-Bonneau P, Malthièry Y, Bonneau D, Reynier P (2007)
840 Mitochondrial coupling defect in Charcot-Marie-Tooth type 2A disease. Ann Neurol 61:315–323.
841 doi: 10.1002/ana.21086

842 34. Luo N, Yue F, Jia Z, Chen J, Deng Q, Zhao Y, Kuang S (2021) Reduced electron transport chain
843 complex I protein abundance and function in Mfn2-deficient myogenic progenitors lead to
844 oxidative stress and mitochondria swelling. FASEB J 35:e21426. doi: 10.1096/fj.202002464R

845 35. Madrid R, Guariglia SR, Haworth A, Korosh W, Gavin M, Lyon GJ (2020) Early-onset cerebellar
846 ataxia in a patient with CMT2A2. Cold Spring Harb Mol Case Stud 6:a005108. doi:
847 10.1101/mcs.a005108

848 36. Marra F, Lunetti P, Curcio R, Lasorsa FM, Capobianco L, Porcelli V, Dolce V, Fiermonte G, Scarcia P
849 (2021) An Overview of Mitochondrial Protein Defects in Neuromuscular Diseases. Biomolecules
850 11:1633. doi: 10.3390/biom11111633

851 37. McDermott H, Sherlaw-Sturrock C, Baptista J, Hartles-Spencer L, Naik S (2022) Rapid exome
852 sequencing in critically ill children impacts acute and long-term management of patients and their
853 families: A retrospective regional evaluation. Eur J Med Genet 65:104571. doi:
854 10.1016/j.ejmg.2022.104571

855 38. McLelland G-L, Goiran T, Yi W, Dorval G, Chen CX, Lauinger ND, Krahn AI, Valimehr S, Rakovic A,
856 Rouiller I, Durcan TM, Trempe J-F, Fon EA (2018) Mfn2 ubiquitination by PINK1/parkin gates the
857 p97-dependent release of ER from mitochondria to drive mitophagy. eLife 7:e32866. doi:
858 10.7554/eLife.32866

859 39. Mick E, Titov DV, Skinner OS, Sharma R, Jourdain AA, Mootha VK Distinct mitochondrial defects
860 trigger the integrated stress response depending on the metabolic state of the cell. eLife 9:e49178.
861 doi: 10.7554/eLife.49178

862 40. Misko A, Jiang S, Wegorzewska I, Milbrandt J, Baloh RH (2010) Mitofusin 2 is necessary for
863 transport of axonal mitochondria and interacts with the Miro/Milton complex. J Neurosci 30:4232–
864 4240. doi: 10.1523/JNEUROSCI.6248-09.2010

865 41. Nicholson GA, Magdelaine C, Zhu D, Grew S, Ryan MM, Sturtz F, Vallat J-M, Ouvrier RA (2008)
866 Severe early-onset axonal neuropathy with homozygous and compound heterozygous MFN2
867 mutations. Neurology 70:1678–1681. doi: 10.1212/01.wnl.0000311275.89032.22

868 42. Pagliarini DJ, Calvo SE, Chang B, Sheth SA, Vafai SB, Ong S-E, Walford GA, Sugiana C, Boneh A, Chen
869 WK, Hill DE, Vidal M, Evans JG, Thorburn DR, Carr SA, Mootha VK (2008) A mitochondrial protein
870 compendium elucidates complex I disease biology. Cell 134:112–123. doi:
871 10.1016/j.cell.2008.06.016

872 43. Pellino G, Faggioli R, Galuppi A, Leon A, Fusco C, Tugnoli V, Suppiej A (2021) Mitofusin 2: The
873 missing link between mtDNA maintenance defects and neurotransmitter disorders. Mitochondrion
874 61:159–164. doi: 10.1016/j.mito.2021.09.011

875 44. Perkins LA, Holderbaum L, Tao R, Hu Y, Sopko R, McCall K, Yang-Zhou D, Flockhart I, Binari R, Shim
876 H-S, Miller A, Housden A, Foos M, Randkelv S, Kelley C, Namgyal P, Villalta C, Liu L-P, Jiang X, Huan-
877 Huan Q, Wang X, Fujiyama A, Toyoda A, Ayers K, Blum A, Czech B, Neumuller R, Yan D, Cavallaro A,
878 Hibbard K, Hall D, Cooley L, Hannon GJ, Lehmann R, Parks A, Mohr SE, Ueda R, Kondo S, Ni J-Q,
879 Perrimon N (2015) The Transgenic RNAi Project at Harvard Medical School: Resources and
880 Validation. Genetics 201:843–852. doi: 10.1534/genetics.115.180208

881 45. Pich S, Bach D, Briones P, Liesa M, Camps M, Testar X, Palacín M, Zorzano A (2005) The Charcot–
882 Marie–Tooth type 2A gene product, Mfn2, up-regulates fuel oxidation through expression of
883 OXPHOS system. Human Molecular Genetics 14:1405–1415. doi: 10.1093/hmg/ddi149

884 46. Polke JM, Laurá M, Pareyson D, Taroni F, Milani M, Bergamin G, Gibbons VS, Houlden H, Chamley
885 SC, Blake J, Devile C, Sandford R, Sweeney MG, Davis MB, Reilly MM (2011) Recessive axonal
886 Charcot-Marie-Tooth disease due to compound heterozygous mitofusin 2 mutations. Neurology
887 77:168–173. doi: 10.1212/WNL.0b013e3182242d4d

888 47. Quirós PM, Mottis A, Auwerx J (2016) Mitonuclear communication in homeostasis and stress. Nat
889 Rev Mol Cell Biol 17:213–226. doi: 10.1038/nrm.2016.23

890 48. Renaldo F, Amati-Bonneau P, Slama A, Romana C, Forin V, Doummar D, Barnerias C, Bursztyn J,
891 Mayer M, Khouri N, Billette de Villemeur T, Burglen L, Reynier P, Bernabe Gelot A, Rodriguez D
892 (2012) MFN2, a new gene responsible for mitochondrial DNA depletion. Brain 135:e223, 1–4;
893 author reply e224, 1–3. doi: 10.1093/brain/aws111

894 49. Rizzo F, Bono S, Ruepp MD, Salani S, Ottoboni L, Abati E, Melzi V, Cordiglieri C, Pagliarani S, De
895 Gioia R, Anastasia A, Taiana M, Garbellini M, Lodato S, Kunderfranco P, Cazzato D, Cartelli D, Lonati
896 C, Bresolin N, Comi G, Nizzardo M, Corti S (2023) Combined RNA interference and gene
897 replacement therapy targeting MFN2 as proof of principle for the treatment of Charcot-Marie-
898 Tooth type 2A. Cell Mol Life Sci 80:373. doi: 10.1007/s00018-023-05018-w

899 50. Rocha AG, Franco A, Krezel AM, Rumsey JM, Alberti JM, Knight WC, Biris N, Zacharioudakis E,
900 Janetka JW, Baloh RH, Kitsis RN, Mochly-Rosen D, Townsend RR, Gavathiotis E, Dorn GW (2018)
901 MFN2 agonists reverse mitochondrial defects in preclinical models of Charcot-Marie-Tooth disease
902 type 2A. Science 360:336–341. doi: 10.1126/science.aao1785

903 51. Rouzier C, Bannwarth S, Chaussenot A, Chevrollier A, Verschueren A, Bonello-Palot N, Fragaki K,
904 Cano A, Pouget J, Pellissier J-F, Procaccio V, Chabrol B, Paquis-Flucklinger V (2012) The MFN2 gene
905 is responsible for mitochondrial DNA instability and optic atrophy “plus” phenotype. Brain 135:23–
906 34. doi: 10.1093/brain/awr323

907 52. Sabouny R, Wong R, Lee-Glover L, Greenway SC, Sinasac DS, Care4Rare Canada, Khan A, Shutt TE
908 (2019) Characterization of the C584R variant in the mtDNA depletion syndrome gene FBXL4,
909 reveals a novel role for FBXL4 as a regulator of mitochondrial fusion. Biochim Biophys Acta Mol
910 Basis Dis 1865:165536. doi: 10.1016/j.bbadis.2019.165536

911 53. Sawyer SL, Cheuk-Him Ng A, Innes AM, Wagner JD, Dyment DA, Tetreault M, Care4Rare Canada
912 Consortium, Majewski J, Boycott KM, Screaton RA, Nicholson G (2015) Homozygous mutations in
913 MFN2 cause multiple symmetric lipomatosis associated with neuropathy. Hum Mol Genet
914 24:5109–5114. doi: 10.1093/hmg/ddv229

915 54. Sharma G, Zaman M, Sabouny R, Joel M, Martens K, Martino D, De Koning APJ, Pfeffer G, Shutt TE
916 (2022) Characterization of a novel variant in the HR1 domain of MFN2 in a patient with ataxia,
917 optic atrophy and sensorineural hearing loss. F1000Res 10:606. doi:
918 10.12688/f1000research.53230.2

919 55. Sidarala V, Zhu J, Levi-D'Ancona E, Pearson GL, Reck EC, Walker EM, Kaufman BA, Soleimanpour SA
920 (2022) Mitofusin 1 and 2 regulation of mitochondrial DNA content is a critical determinant of
921 glucose homeostasis. Nat Commun 13:2340. doi: 10.1038/s41467-022-29945-7

922 56. Silva Ramos E, Motori E, Brüser C, Kühl I, Yeroslaviz A, Ruzzenente B, Kauppila JHK, Busch JD,
923 Hultenby K, Habermann BH, Jakobs S, Larsson N-G, Mourier A (2019) Mitochondrial fusion is
924 required for regulation of mitochondrial DNA replication. PLoS Genet 15:e1008085. doi:
925 10.1371/journal.pgen.1008085

926 57. Tan CA, Rabideau M, Blevins A, Westbrook MJ, Ekstein T, Nykamp K, Deucher A, Harper A, Demmer
927 L (2016) Autosomal recessive MFN2-related Charcot-Marie-Tooth disease with diaphragmatic
928 weakness: Case report and literature review. Am J Med Genet A 170:1580–1584. doi:
929 10.1002/ajmg.a.37611

930 58. UniProt Consortium (2023) UniProt: the Universal Protein Knowledgebase in 2023. Nucleic Acids
931 Res 51:D523–D531. doi: 10.1093/nar/gkac1052

932 59. Valente AJ, Maddalena LA, Robb EL, Moradi F, Stuart JA (2017) A simple ImageJ macro tool for
933 analyzing mitochondrial network morphology in mammalian cell culture. Acta Histochem 119:315–
934 326. doi: 10.1016/j.acthis.2017.03.001

935 60. Vielhaber S, Debska-Vielhaber G, Peeva V, Schoeler S, Kudin AP, Minin I, Schreiber S, Dengler R,
936 Kollewe K, Zuschratter W, Kornblum C, Zsurka G, Kunz WS (2013) Mitofusin 2 mutations affect
937 mitochondrial function by mitochondrial DNA depletion. Acta Neuropathol 125:245–256. doi:
938 10.1007/s00401-012-1036-y

939 61. Winter JM, Yadav T, Rutter J (2022) Stressed to death: Mitochondrial stress responses connect
940 respiration and apoptosis in cancer. Mol Cell 82:3321–3332. doi: 10.1016/j.molcel.2022.07.012

941 62. Zacharioudakis E, Agianian B, Kumar MV V, Biris N, Garner TP, Rabinovich-Nikitin I, Ouchida AT,
942 Margulets V, Nordstrøm LU, Riley JS, Dolgalev I, Chen Y, Wittig AJH, Pekson R, Mathew C, Wei P,
943 Tsirigos A, Tait SWG, Kirshenbaum LA, Kitsis RN, Gavathiotis E (2022) Modulating mitofusins to
944 control mitochondrial function and signaling. Nat Commun 13:3775. doi: 10.1038/s41467-022-
945 31324-1

946 63. Zaman M, Sharma G, Almutawa W, Soule TG, Sabouny R, Joel M, Mohan A, Chute C, Joseph JT,
947 Pfeffer G, Shutt TE (2025) The MFN2 Q367H variant reveals a novel pathomechanism connected to
948 mtDNA-mediated inflammation. Life Sci Alliance 8:e202402921. doi: 10.26508/lsa.202402921

949 64. Zaman M, Shutt TE (2022) The Role of Impaired Mitochondrial Dynamics in MFN2-Mediated
950 Pathology. Front Cell Dev Biol 10:858286. doi: 10.3389/fcell.2022.858286

951 65. Züchner S, De Jonghe P, Jordanova A, Claeys KG, Guergueltcheva V, Cherninkova S, Hamilton SR,
952 Van Stavern G, Krajewski KM, Stajich J, Tournev I, Verhoeven K, Langerhorst CT, de Visser M, Baas

953 F, Bird T, Timmerman V, Shy M, Vance JM (2006) Axonal neuropathy with optic atrophy is caused
954 by mutations in mitofusin 2. Ann Neurol 59:276–281. doi: 10.1002/ana.20797

955 66. Zurita Rendón O, Antonicka H, Horvath R, Shoubridge EA (2016) A Mutation in the Flavin Adenine
956 Dinucleotide-Dependent Oxidoreductase FOXRED1 Results in Cell-Type-Specific Assembly Defects
957 in Oxidative Phosphorylation Complexes I and II. Mol Cell Biol 36:2132–2140. doi:
958 10.1128/MCB.00066-16

(a)

Arginine 334

317 355

```
MFN2_HUMAN        AQGMPEGGGALAEGFQVRMFEFQNFERRFEECISQSAVK
MFN1_HUMAN        AQGMPESGVALAEGFHARLQEFQNFEQIFEECISQSAVK
MFN2_MOUSE        AQGMPEGGGALAEGFQVRMFEFQNFERQFEECISQSAVK
MFN2_FISH         AQGMPEAGGALAEGFQARMFEFQNFERRFEECISQSAVK
MFN_FRUITFLY_Tr   AKGNPPHMGAIAEGFQIRYFEFQDFERKFEECISQSAVK
MFN_WORM_Transm   ARGLVQK-AYQAEGHGTRALEFQNFERHFEHCISRSAIH

cons              :      ***.  *  ***:**: **.***:**::
```

(b)

Isoleucine 485

475 486

```
FXRD1_HUMAN       YLGEKIQENNI--I
FXRD1_MOUSE       YLGEKLQEYNI--L
FXRD1_FISH        IKKKPILERNI--V
FXRD1_FRUITFLY    IVDQPMFELNNVLS
FXRD1_WORM        LRGKTVKPECF--

cons                  : :
```

(c)

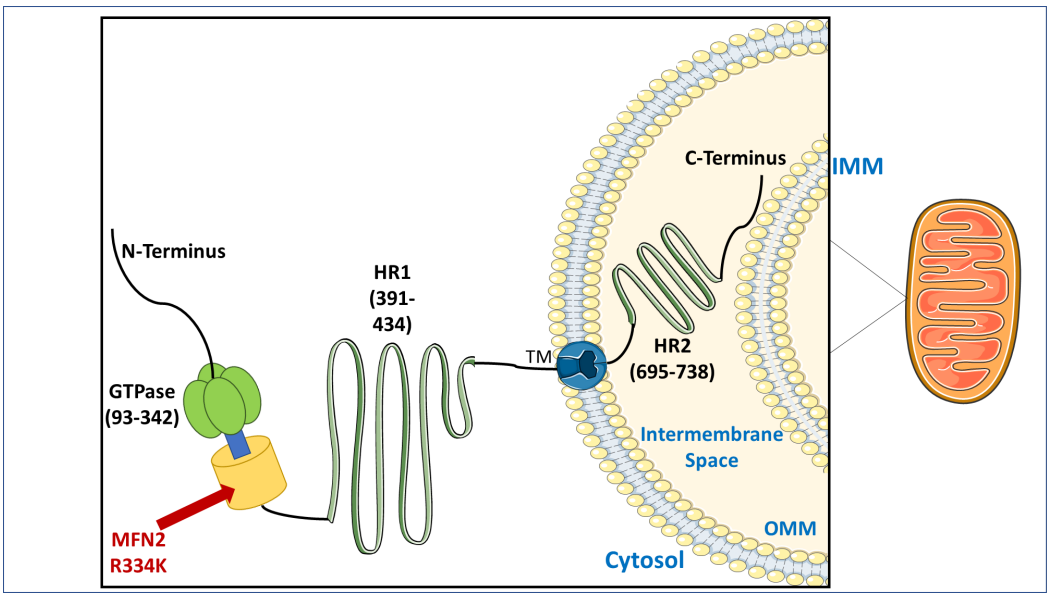

Figure 1

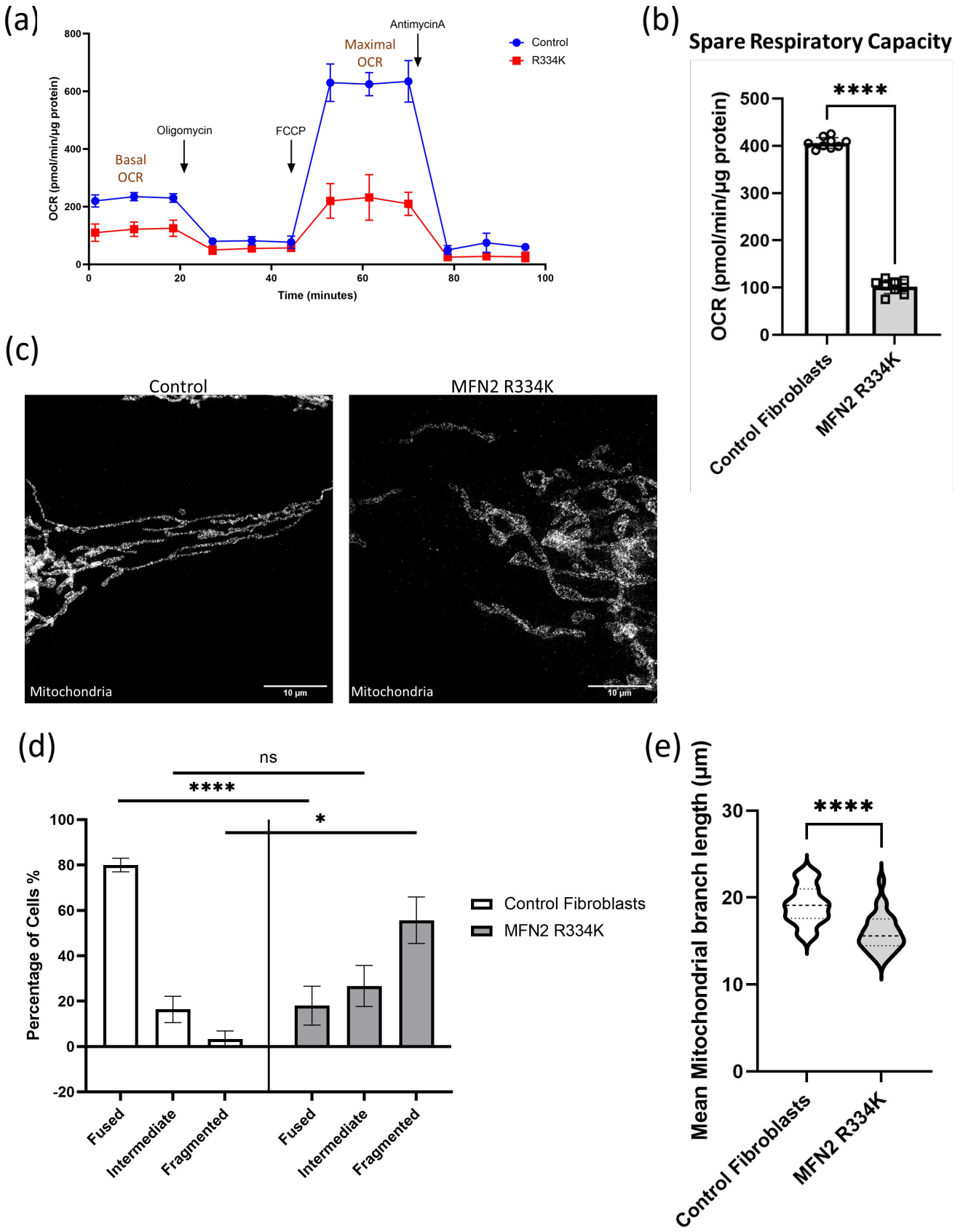
(a)
OCR (pmol/min/µg protein)
Time (minutes)
Basal OCR
Oligomycin
FCCP
Maximal OCR
AntimycinA
Control
R334K
(b)
Spare Respiratory Capacity
OCR (pmol/min/µg protein)
****
Control Fibroblasts
MFN2 R334K
(c)
Control
MFN2 R334K
Mitochondria
10 µm
(d)
ns
****
*
Percentage of Cells %
Fused
Intermediate
Fragmented
Control Fibroblasts
MFN2 R334K
(e)
Mean Mitochondrial branch length (µm)
****
Control Fibroblasts
MFN2 R334K

Figure 2

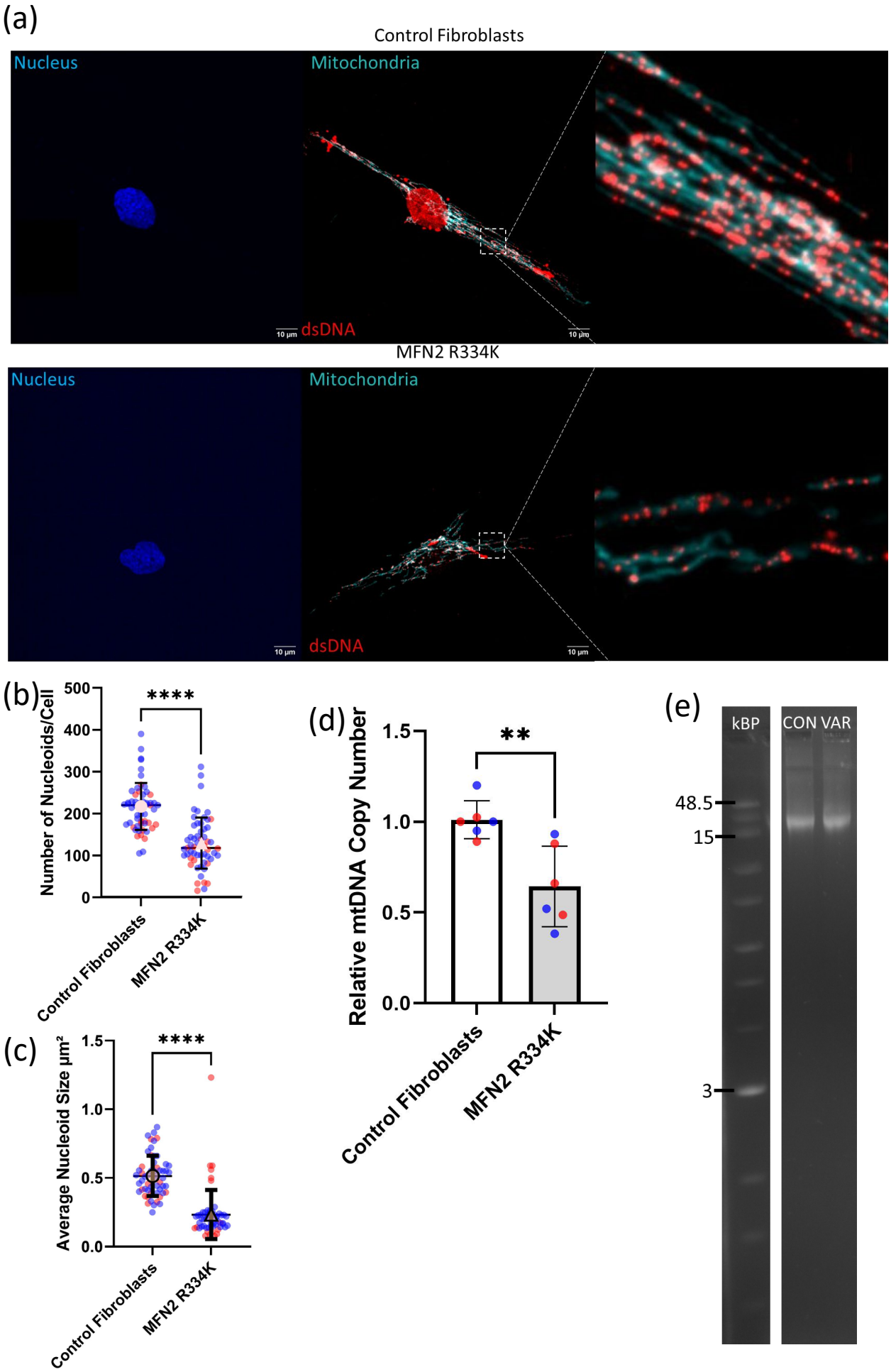
(a)
Control Fibroblasts
Nucleus
Mitochondria
dsDNA
10 µm
MFN2 R334K
Nucleus
Mitochondria
dsDNA
10 µm
(b)
Number of Nucleoids/Cell
500
400
300
200
100
0
****
Control Fibroblasts
MFN2 R334K
(c)
Average Nucleoid Size µm²
1.5
1.0
0.5
0.0
****
Control Fibroblasts
MFN2 R334K
(d)
Relative mtDNA Copy Number
1.5
1.0
0.5
0.0
**
Control Fibroblasts
MFN2 R334K
(e)
kBP
CON VAR
48.5
15
3

Figure 3

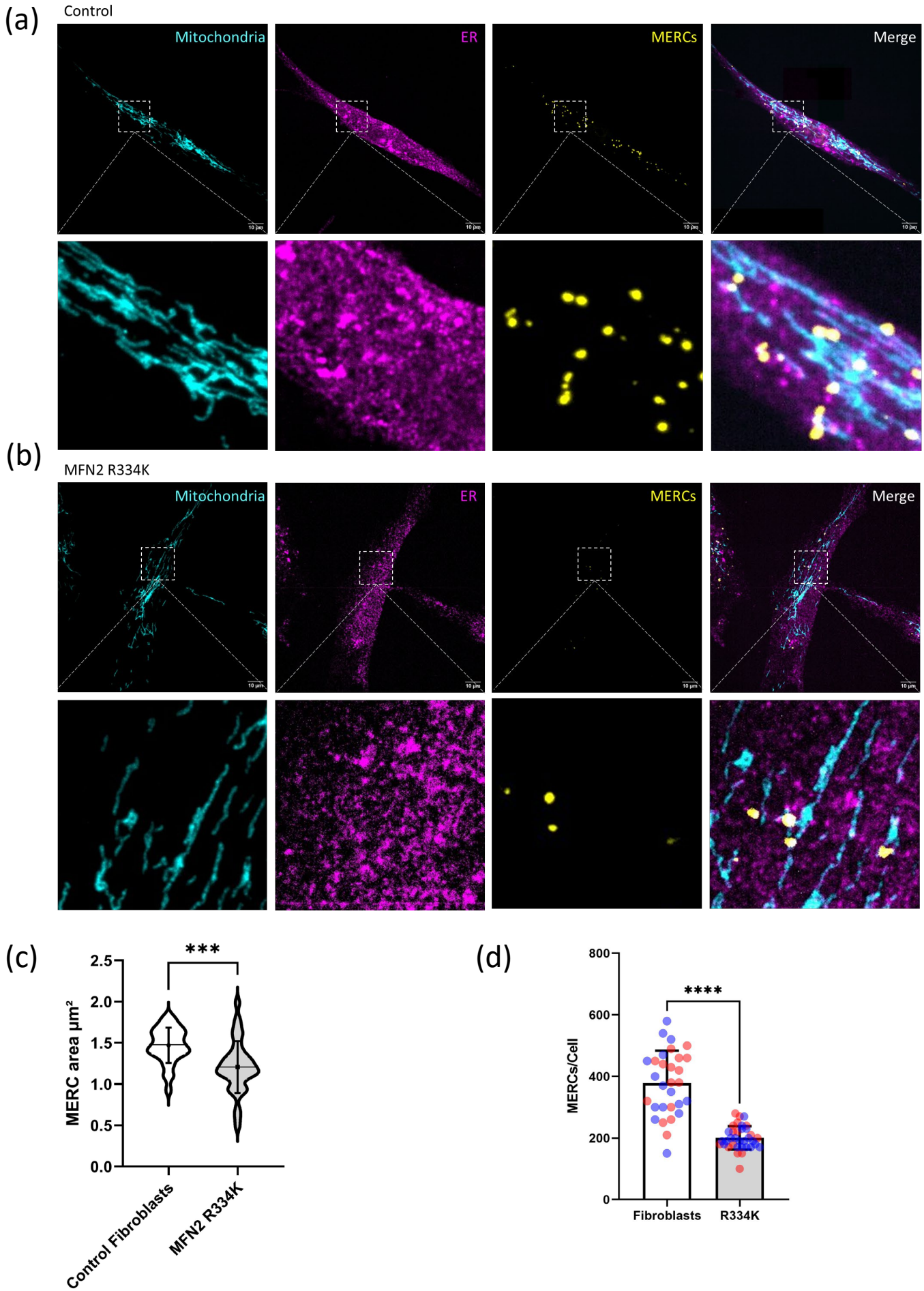
(a)
Control
Mitochondria
ER
MERCs
Merge
(b)
MFN2 R334K
Mitochondria
ER
MERCs
Merge
(c)
***
MERC area µm²
2.5
2.0
1.5
1.0
0.5
0.0
Control Fibroblasts
MFN2 R334K
(d)
****
MERCs/Cell
800
600
400
200
0
Fibroblasts
R334K

Figure 4

(a)

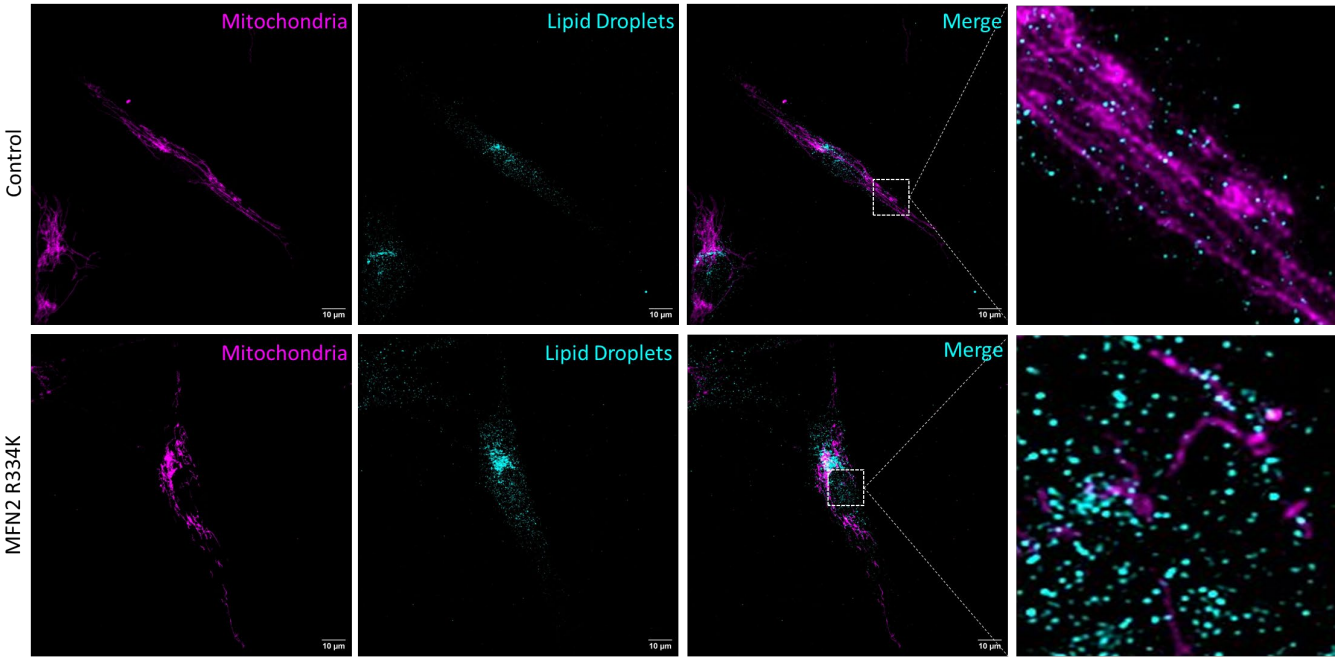
Mitochondria
Lipid Droplets
Merge
Control
MFN2 R334K

(b)

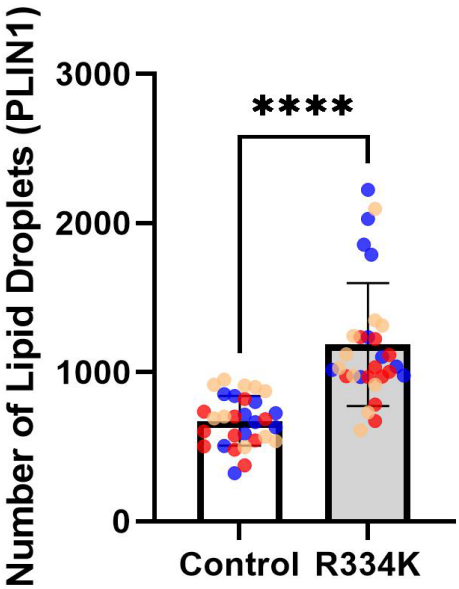
Number of Lipid Droplets (PLIN1)
3000
2000
1000
0
****
Control
R334K

(c)

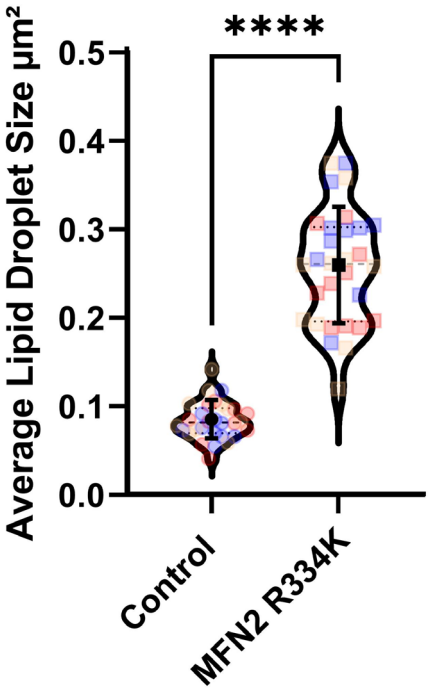
Average Lipid Droplet Size µm²
0.5
0.4
0.3
0.2
0.1
0.0
****
Control
MFN2 R334K

Figure 5

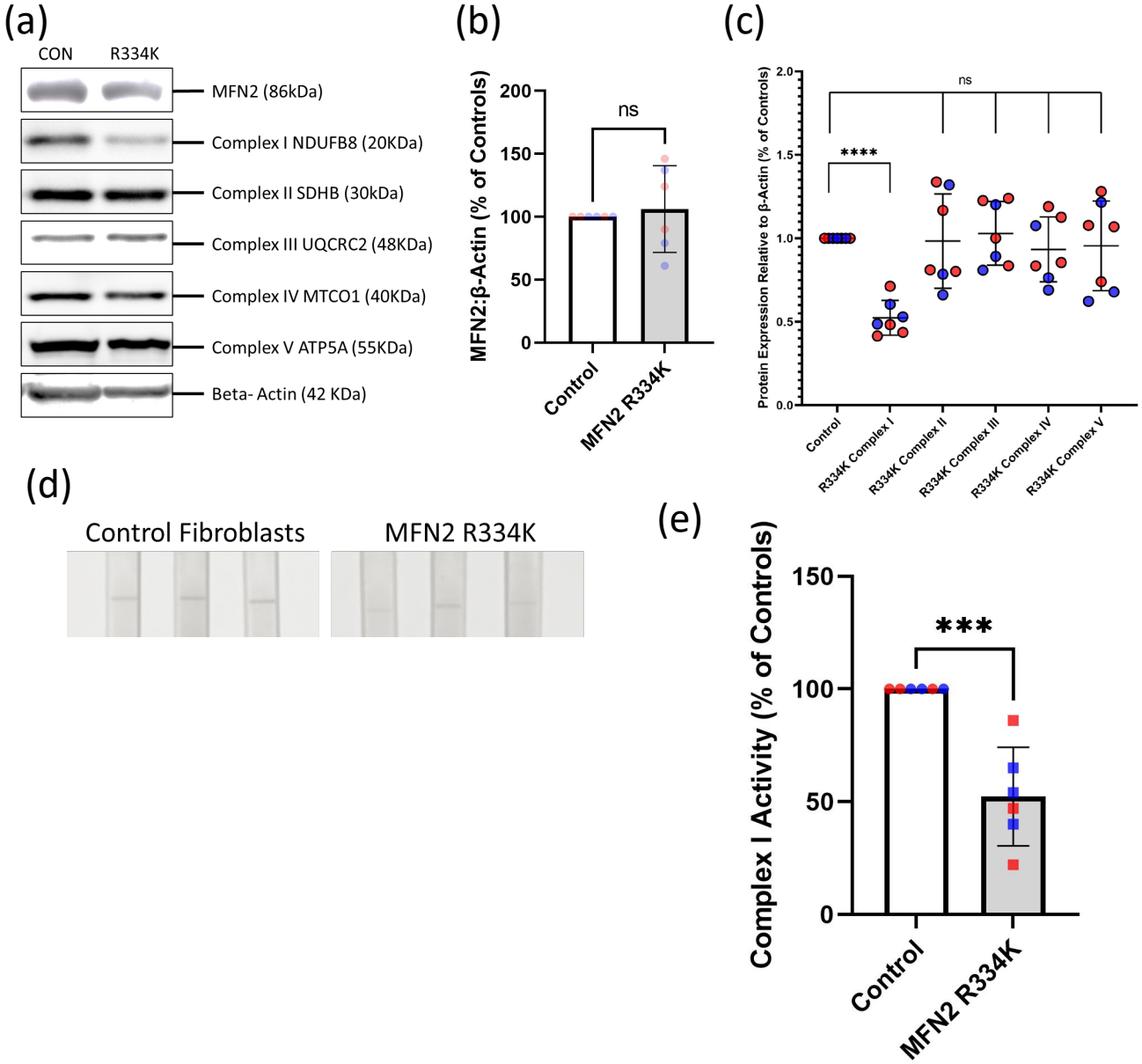
(a)
CON
R334K
MFN2 (86kDa)
Complex I NDUFB8 (20KDa)
Complex II SDHB (30kDa)
Complex III UQCRC2 (48KDa)
Complex IV MTCO1 (40KDa)
Complex V ATP5A (55KDa)
Beta- Actin (42 KDa)
(b)
MFN2:β-Actin (% of Controls)
200
150
100
50
0
ns
Control
MFN2 R334K
(c)
Protein Expression Relative to β-Actin (% of Controls)
2.0
1.5
1.0
0.5
0.0
ns
****
Control
R334K Complex I
R334K Complex II
R334K Complex III
R334K Complex IV
R334K Complex V
(d)
Control Fibroblasts
MFN2 R334K
(e)
Complex I Activity (% of Controls)
150
100
50
0
***
Control
MFN2 R334K

Figure 6

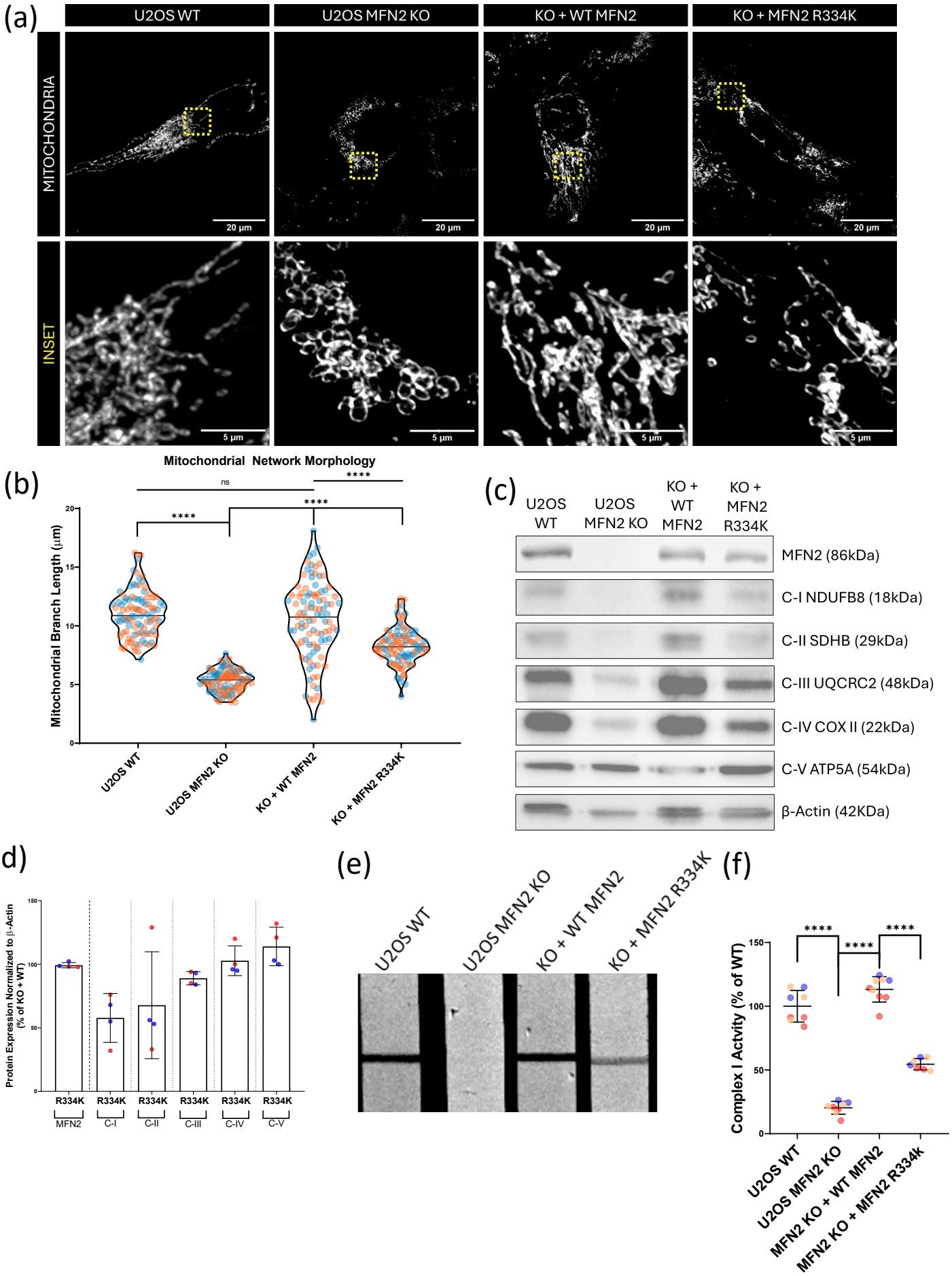
(a)
U2OS WT
U2OS MFN2 KO
KO + WT MFN2
KO + MFN2 R334K
MITOCHONDRIA
INSET
20 µm
5 µm
(b)
Mitochondrial Network Morphology
Mitochondrial Branch Length (µm)
ns
****
U2OS WT
U2OS MFN2 KO
KO + WT MFN2
KO + MFN2 R334K
(c)
U2OS WT
U2OS MFN2 KO
KO + WT MFN2
KO + MFN2 R334K
MFN2 (86kDa)
C-I NDUFB8 (18kDa)
C-II SDHB (29kDa)
C-III UQCRC2 (48kDa)
C-IV COX II (22kDa)
C-V ATP5A (54kDa)
β-Actin (42KDa)
(d)
Protein Expression Normalized to β-Actin (% of KO + WT)
R334K
MFN2
C-I
C-II
C-III
C-IV
C-V
(e)
U2OS WT
U2OS MFN2 KO
KO + WT MFN2
KO + MFN2 R334K
(f)
Complex I Activity (% of WT)
U2OS WT
U2OS MFN2 KO
MFN2 KO + WT MFN2
MFN2 KO + MFN2 R334k

Figure 7

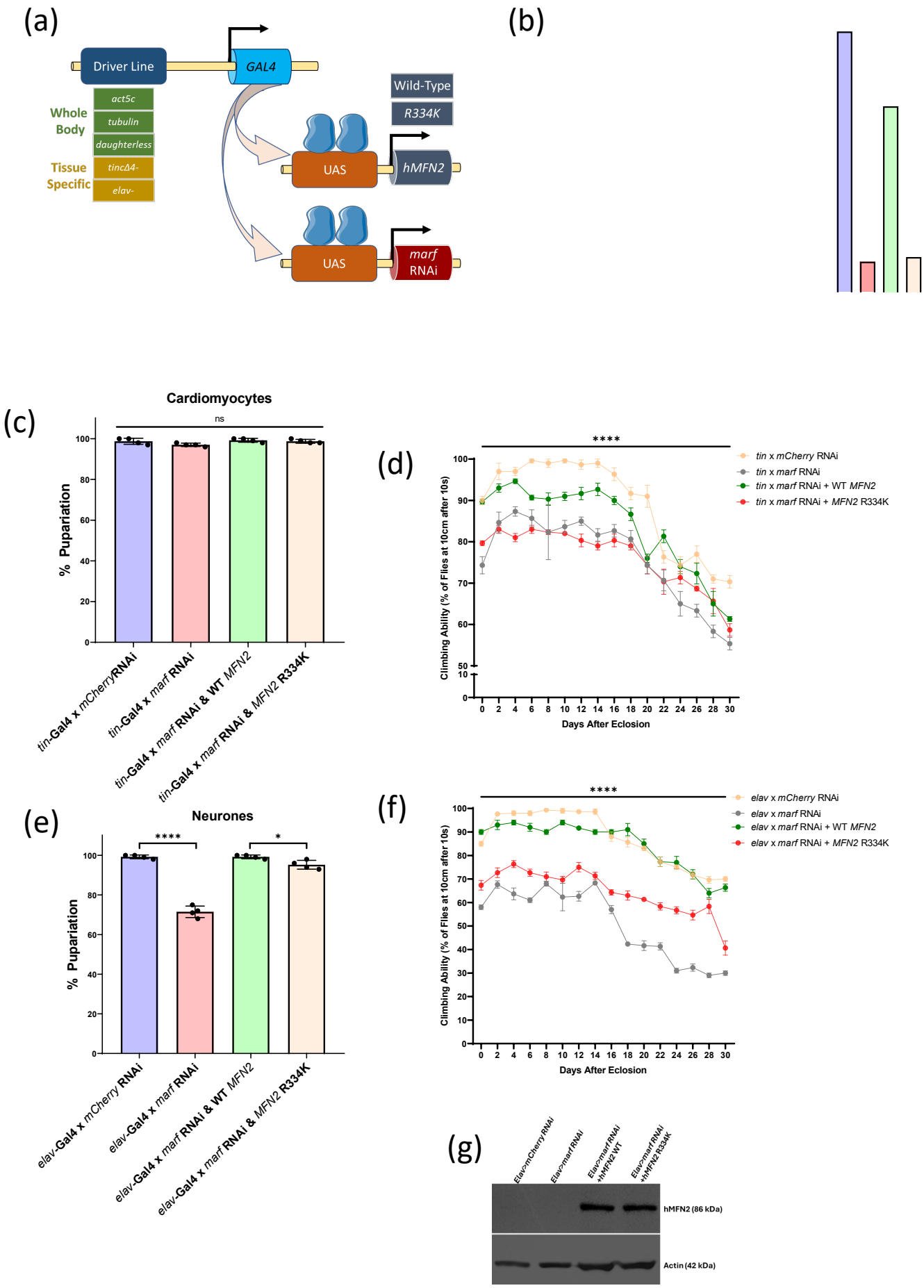
(a)
Driver Line
GAL4
Whole Body
act5c
tubulin
daughterless
Tissue Specific
tincΔ4-
elav-
Wild-Type
R334K
UAS
hMFN2
UAS
marf RNAi
(b)
(c)
Cardiomyocytes
ns
% Pupariation
tin-Gal4 x mCherryRNAi
tin-Gal4 x marf RNAi
tin-Gal4 x marf RNAi & WT MFN2
tin-Gal4 x marf RNAi & MFN2 R334K
(d)
****
Climbing Ability (% of Flies at 10cm after 10s)
Days After Eclosion
tin x mCherry RNAi
tin x marf RNAi
tin x marf RNAi + WT MFN2
tin x marf RNAi + MFN2 R334K
(e)
Neurones
****
*
% Pupariation
elav-Gal4 x mCherry RNAi
elav-Gal4 x marf RNAi
elav-Gal4 x marf RNAi & WT MFN2
elav-Gal4 x marf RNAi & MFN2 R334K
(f)
****
Climbing Ability (% of Flies at 10cm after 10s)
Days After Eclosion
elav x mCherry RNAi
elav x marf RNAi
elav x marf RNAi + WT MFN2
elav x marf RNAi + MFN2 R334K
(g)
Elav>mCherry RNAi
Elav>marf RNAi
Elav>marf RNAi +hMFN2 WT
Elav>marf RNAi +hMFN2 R334K
hMFN2 (86 kDa)
Actin (42 kDa)

Figure 8

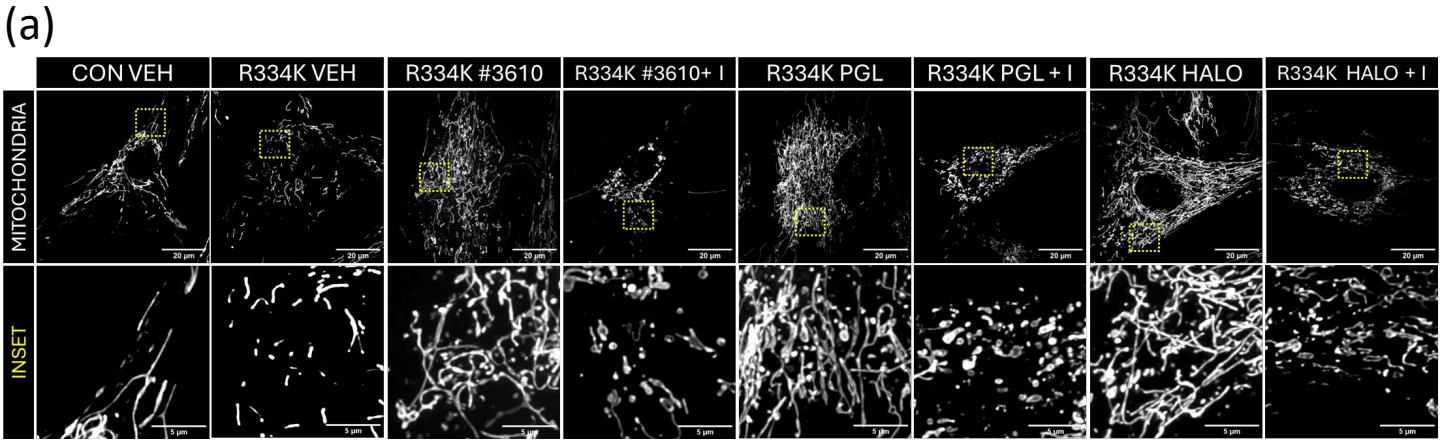
(a)
CON VEH
R334K VEH
R334K #3610
R334K #3610+ I
R334K PGL
R334K PGL + I
R334K HALO
R334K HALO + I
MITOCHONDRIA
INSET

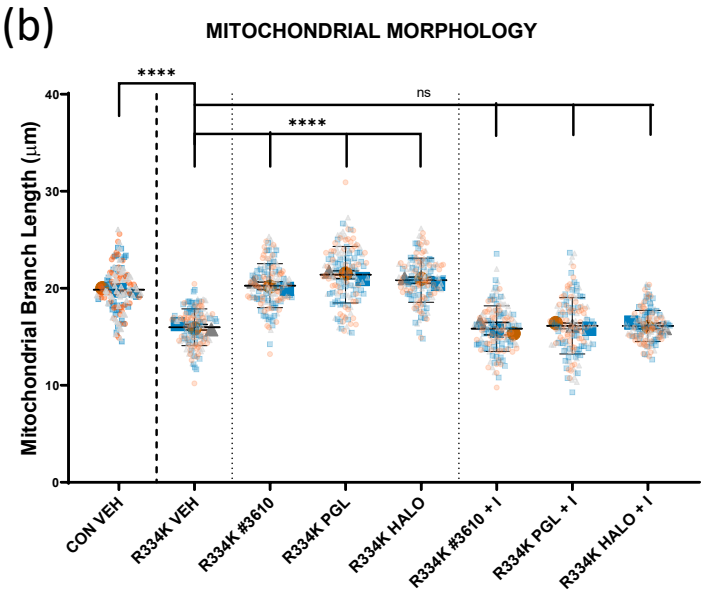
(b)
MITOCHONDRIAL MORPHOLOGY
Mitochondrial Branch Length (μm)
****
****
ns
CON VEH
R334K VEH
R334K #3610
R334K PGL
R334K HALO
R334K #3610 + I
R334K PGL + I
R334K HALO + I

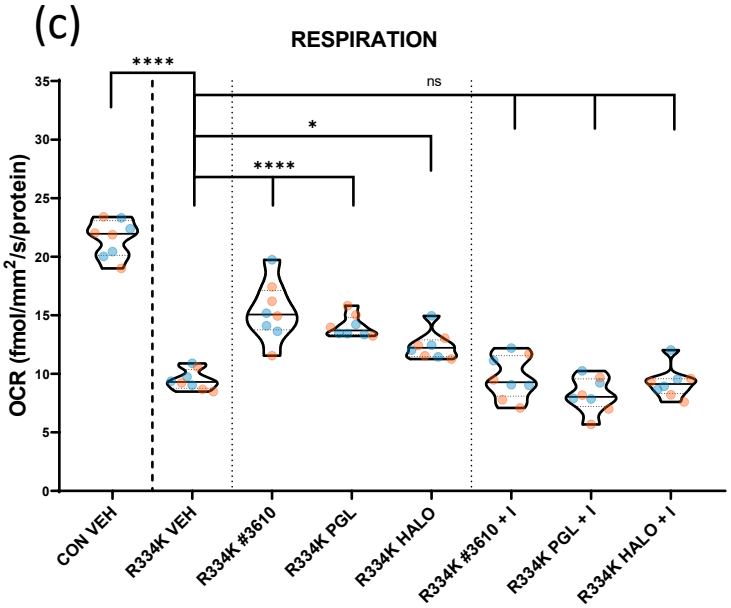
(c)
RESPIRATION
OCR (fmol/mm²/s/protein)
****
*
****
ns
CON VEH
R334K VEH
R334K #3610
R334K PGL
R334K HALO
R334K #3610 + I
R334K PGL + I
R334K HALO + I

Figure 9

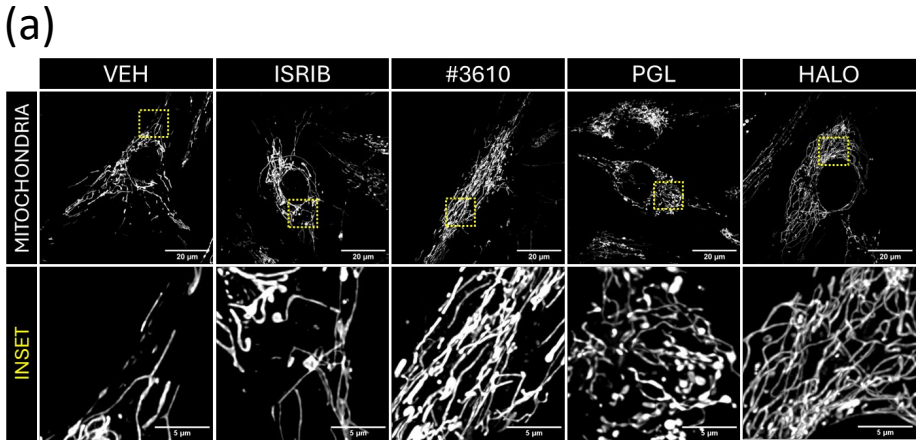

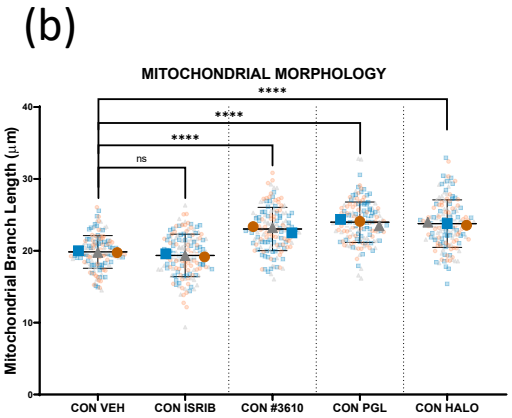

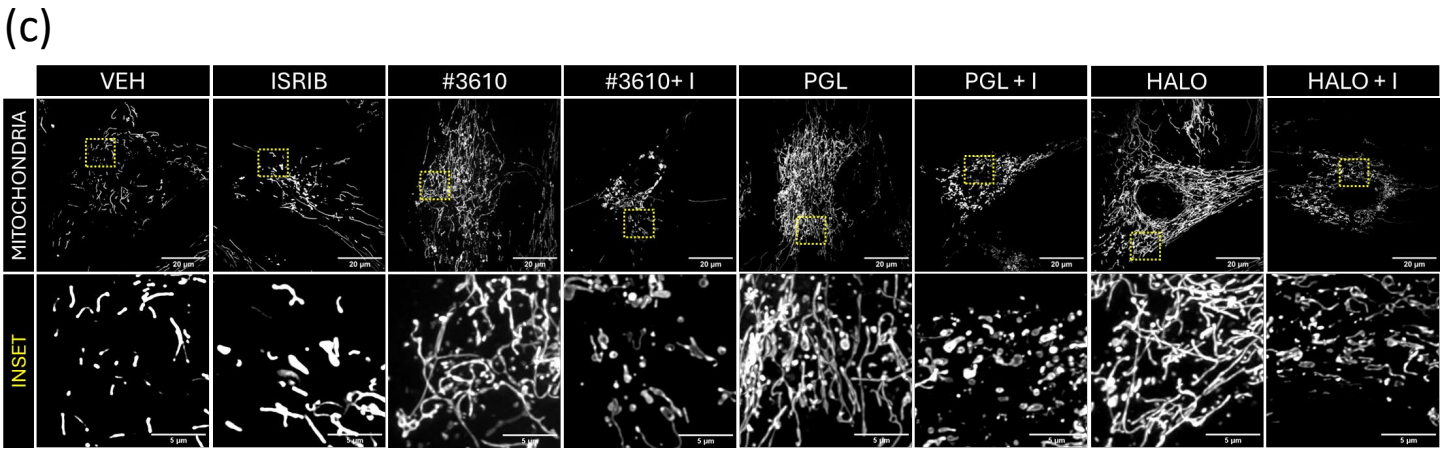

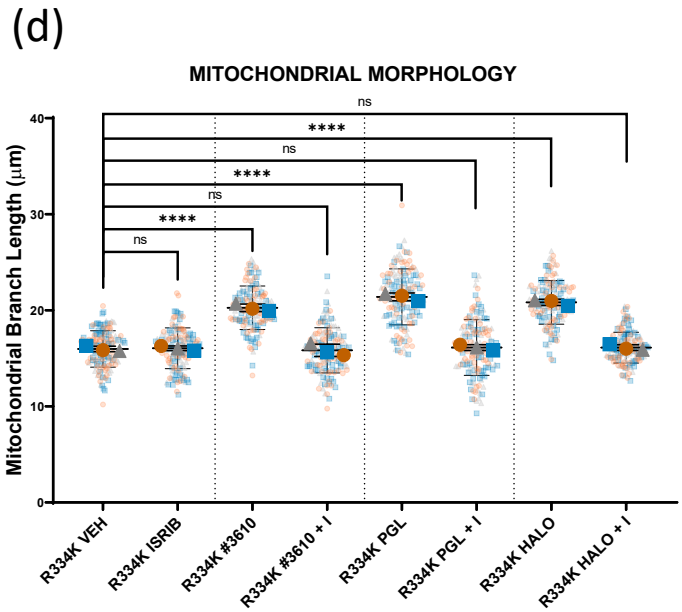

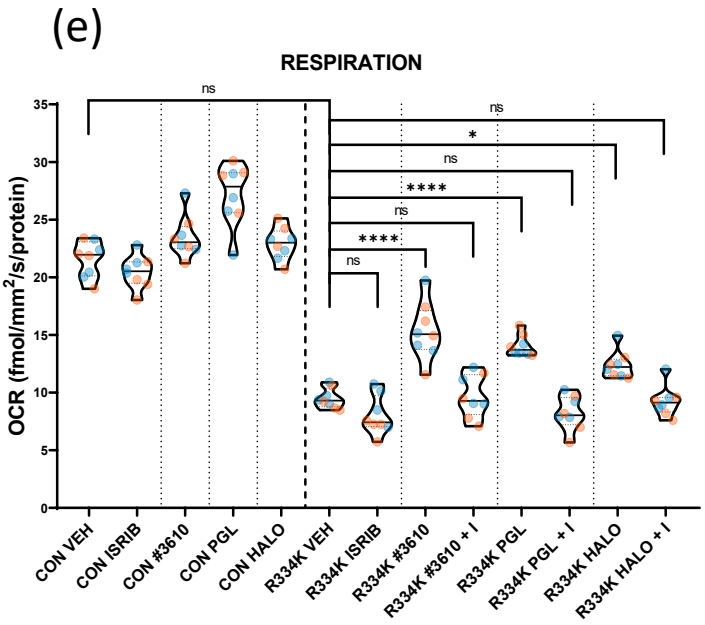

Supplemental Figure S1